Edinburgh Research Explorer

Tensile behaviour of pitting corroded steel bars

Tensile behaviour of pitting corroded steel bars: laboratory investigation and probabilistic-based analysis

Yifan Liu [a], Hao Yuan [a], Zhiwei Miao [a]*, Xiangdong Geng [a],

Xinxing Shao [a], Yong Lu [b]

[a] *Key Laboratory of Concrete and Pre-stressed Concrete Structures of China Ministry of Education, Southeast University, Nanjing 210096, PR China.*

[b] *Institute for Infrastructure and Environment, School of Engineering, The University of Edinburgh, The King's Buildings, Edinburgh EH9 3JL, UK*

* Corresponding author. *E-mail address*: miaozhiwei@seu.edu.cn

ABSTRACT

Localised corrosion in steel bars has been a long-standing issue in the durability of reinforced concrete structures, but a comprehensive scheme for the analysis of pitting corroded steel bars, especially with respect to the deformation capacity, is not currently available. In this study, the morphological characteristics of 27 pitting steel bars were captured using a 3D scanner. The measured data were used to establish the probability distribution model of the cross-sectional areas of the corroded bars. Uniaxial tensile tests were conducted, and the evolving deformation field of the corroded bars was recorded through Digital Image Correlation (DIC). Based on the 3D reconstructed model and DIC results, an analytical method for evaluating the mechanical properties of pitting steel bars was developed and validated. The results show that the two-component Gaussian mixture distribution model outperforms conventional unimodal distribution models. Comparison of the analytical results with experimental data demonstrates that the proposed procedure is capable of predicting not only the ultimate strength but also the gauge length-dependent ultimate strain of corroded bars. Additionally, there exists a strengthening effect in the ultimate stress at the critical sections and this effect should not be ignored for accurate predictions.

KEYWORDS

Pitting corrosion; Mechanical properties; Gaussian mixture model; 3D scanning; Digital Image Correlation.

1 Introduction

Corrosion of reinforcement in concrete is a primary risk to the reliability and durability of structures. Especially for coastal buildings that have been subjected to erosion in a marine environment for a long time, severe localised corrosion, or in other words pitting, on the surface of steel reinforcing bars has been reported in previous investigations [1, 2]. Compared with general corrosion, pitting corrosion leads to significant deterioration of the tensile strength and a sharp reduction of the deformation capacity of the reinforcement. Such deterioration in the mechanical properties of the reinforcement significantly impairs the overall seismic performance of the structure.

For effective maintenance and retrofitting of corroded structures, it is essential to be able to accurately estimate the residual performance of RC components or structures. Some researchers have attempted to directly characterize the geometric changes in corroded rebar at the component or structural level. Stewart [3-5], for instance, discretized RC structures into a series of elements, each containing unique pitting information such as pit depth, to assess structural reliability and vulnerability. Their findings suggested that the mechanical behaviour of these rebar segments has a significant impact on the outcome of structural analysis. Akiyama and co-workers [6-11] employed a reduced cross-sectional area approach in finite element simulations to account for corrosion-induced degradation. While this method has achieved satisfactory results in the assessment of the load-bearing capacity, their finite element analysis still showed discrepancies with experimental results when it comes to deformation capacity, mainly because they did not consider the degradation of ductility in corroded rebar units. Thus, there is still a need for a material-level assessment of residual mechanical properties of corroded rebar, especially in terms of deformation capacity [12-14].

The issue of reinforcement corrosion has attracted broad interest in recent decades, and some important characteristics have been generally recognized among researchers. For instance, the nominal yield strength and nominal ultimate strength of reinforcement (i.e. the ratio of tensile force to the original cross-sectional area) decrease linearly with the increase of corrosion level [15-18], but the true yield strength and ultimate strength of reinforcement (i.e. the ratio of tensile force to the actual minimum cross-sectional area) are not affected and tend to even slightly increase in case of a high corrosion level [17-19]. On the other hand, however, the deformation capacity of non-uniform corroded steel bars has not been satisfactorily addressed in quantitative terms so far. The challenges to this include the following:

i) There is no unified index to quantify the deformation capacity of corroded bars. Most existing studies adopted ultimate strain to represent the deformation capacity of reinforcement, i.e., the average elongation in a specific measured length (referred to as the gauge length). However, various gauge lengths have been used by different researchers to determine the ultimate strain of corroded specimens, such as 50mm [15, 16], 100 mm [20], 200 mm [17], and five times [21] or ten times the diameter of the steel bar [22], or even the total length of the tested reinforcement [18]. In fact, due to uneven distribution of pitting, the axial tensile deformation is locally concentrated in the largest corrosion pits. Consequently, different ultimate strains can result from using different gauge lengths. Therefore, using ultimate strain that is associated with a specific gauge length as a property to evaluate the deformation capacity of non-uniform corroded bars is fundamentally flawed.

ii) The corrosion morphology, reinforcement type as well as diameter all influence the residual capacities of the corroded bars; however, these factors have generally been ignored in the previous studies. Consequently, the degradation models of the strength and deformation capacities, with the model coefficients being derived by regression analysis of experimental data, vary significantly from different studies [23, 24].

As advanced optical technologies like X-ray [7, 11, 25] and 3D scanning [26-28]

techniques gain wider application in civil engineering, recent studies have emerged that utilize these methods to assess the morphological features of corroded bars. Akiyama and co-workers [7, 11, 25] used X-ray and digital image processing techniques to observe the evolution of rebar corrosion inside RC components so as to quantify the spatial growth processes of steel corrosion across the length of a RC member [6-10]. However, the mechanical performance of a whole piece of corroded rebar is largely determined by its most severely corroded section, especially within the plastic hinge region. As such, due to the premature failure of the pitting sections, the full mechanical performance of rebar in the remaining portion is often not reached. Therefore, more refined investigations are required to characterize the morphology of severe localized corrosion in the rebar and the corresponding mechanical performances.

There have been some latest reports on the use of 3D scanners to measure the morphological characteristics of corroded bars. Kashani et al. [27] conducted a corrosion pattern analysis based on the morphological data in which the interference from the ribs was eliminated through signal processing, then concluded that the lognormal distribution model was capable of reflecting the non-uniformity of the residual sections along the length of bars. Tahershamsi et al. [28] applied the cubic splines to get rid of the fluctuation of the cross-sectional area as a result of the ribs, and further analysed the data based on the fitted curves. Zhang et al. [24] also studied the scanned residual sectional area of bars but did not remove the influence of ribs. Their results indicated that the probability distribution of the residual cross-sectional areas of corroded steel bars was not unique; with the increase of the corrosion degree it appeared to change from a normal distribution to a logarithmic normal distribution or a sinusoidal distribution, and eventually back to a normal distribution. Tang et al. [18] observed that the mixed normal distributions with one, two and three modes fitted well the histograms for the corroded steel bars. Although such distributions were supported by the statistical test, their application scenarios were still limited due to poor generalization ability.

In addition to the differences in data processing methods, some of the experimental studies available from the literature [29, 30] adopted a laboratory simulated corrosion process by inducing a direct electric current in the bare bars to prepare the corroded specimens. Such an accelerated corrosion process tends to produce a rather uniform corrosion pattern [30]. It is true that some corrosion scenes in the natural environment do resemble a uniform corrosion pattern. However, corroded steel bar samples extracted from structures that have been in service for decades showed a mixed morphology with a combination of uniform and pitting corrosions [16, 21]. In fact, this mixed pattern of corrosion is common in real RC structures [31-35]. Many studies have proven that the localised corrosion pattern of steel bars is a more critical and hazardous scenario than uniform corrosion [36, 37]. However, there is still a lack of comprehensive investigation on significantly non-uniform corroded specimens containing noticeable corrosion pits. As a result, the unimodal probability distribution model proposed in previous studies based on laboratory experiments cannot represent realistically a pitting corrosion morphology.

In this paper, a comprehensive study on the correlation between the pitting

corrosion morphology and the residual mechanical properties of corroded bars is presented. A set of mixture probability distribution models are developed to quantitatively characterise the pitting corrosion morphology along the steel bars and establish the relationship with the residual mechanical performance of corroded bars. In the study, firstly 27 pitting corrosion steel bars were produced by the semi-immersion electrified method, and then a 3D optical scanner was employed to measure the surface morphological features. A Gaussian mixture model (GMM) was adopted to describe the effective cross-sectional area of the non-uniform corroded bars, and the parameters of the GMM was determined from the experimental data using the Expectation-Maximization (EM) algorithm. Meanwhile, tensile tests were carried out to determine the mechanical properties of the corroded bars. The Digital Image Correlation (DIC) technique was employed to capture the detailed deformation field of the corroded bars during the tensile process. In conjunction with the DIC results, an analytical method for the calculation of the residual mechanical properties of the corroded bars considering the corrosion geometrical profiles was proposed. The proposed method was verified against the experimental data and compared with other degradation prediction models. Finally, a regression analysis of the GMM parameters was carried out, and a general flowchart was provided for the estimation of the residual performance of corroded bars in the entire lifecycle.

2 Experimental program

2.1 Accelerated corrosion procedure

In laboratory experiments, both low-current wet-dry cycling and semi-immersion galvanostatic methods have been found to induce significantly non-uniform corrosion on steel bars [38, 39]. As the primary aim of this study has been focused on the degradation of mechanical properties of corroded steel bars, rather than examining bond degradation or the correlation between corrosion levels and crack width in concrete, the semi-immersion accelerated corrosion method was selected to achieve the desired level of corrosion in a shorter time. Fig. 1(a) shows the overall configuration of the accelerated corrosion setup.

For this investigation, 30 "reinforced" concrete (RC) specimens of the same gross dimension, 150×150×300 mm, were prepared. The RC specimens were cast with C30 concrete. The specific proportions of the concrete mix are listed in Table 1. The steel bars were embedded in concrete with a nominal top cover of 20 mm. The steel bars had an extended portion of 50mm at both ends to connect the anode of DC power. Hot-rolled ribbed steel bars HRB400 were adopted. All steel bars had the same length of 400mm, with three different nominal diameters, namely 8 mm, 16 mm, and 25 mm. There were 10 bars in each diameter group. The corrosion region of all bars had the same length of 200mm, while a protected region of 100mm was set at each end of the bars to facilitate clamping in the later tensile test. The treated steel bars are shown in Fig. 1(b).

Table 1. Mixing proportions for concrete.

Water-binder Ratio	Sand ratio	Cement	Flyash	Mineral fines	Water	Sand	Crushed stone	Admixture
(/)	(/)	(kg/m³)	(kg/m³)	(kg/m³)	(kg/m³)	(kg/m³)	(kg/m³)	(kg/m³)
0.49	0.42	249	46	60	174	765	1045	6.04

As shown in Fig. 1, each specimen was placed horizontally in a plastic tank and the bottom of the specimen was raised by two wooden blocks. A stainless steel mesh was positioned directly underneath and connected to the power cathode. Then the chloride solution (of 5% NaCl concentration) was injected into the tank, and the liquid level was kept 50 mm below the embedded bar.

The corrosion conditions were designed with an aim to achieve three corrosion levels among all the steel bars, namely level A, B, and C, with a target corrosion rate (μ_t) being 10%, 20%, and 30%, respectively. To account for the uncertainty of corrosion, 3 specimens (marked as 1, 2, and 3) were prepared for each diameter of steel bars and at each corrosion level. Thus, for diameter 25mm steel bars at corrosion level of 10% (level A), the first specimen is designated as 25A1, the second specimen 25A2, and so forth.
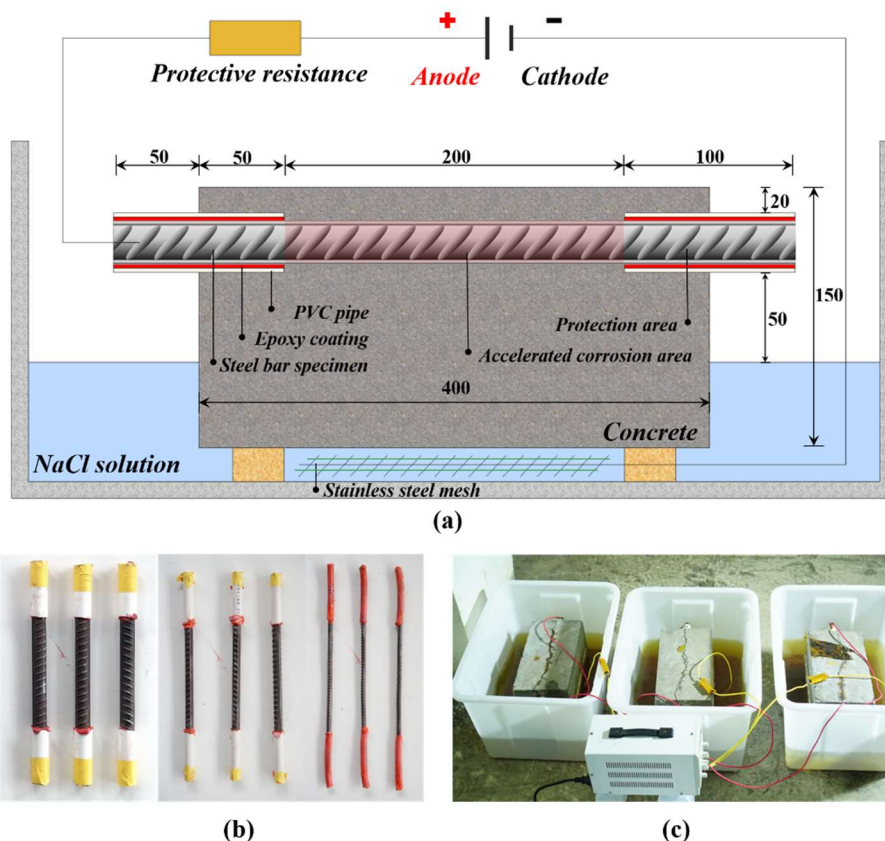

Fig. 1. Schematic diagram of the semi-immersion accelerated corrosion: (a) Elevation view (b) Preparation of steel bars before casting (c) Corrosion in progress.

In order to achieve the three targeted corrosion levels, the electrified time was initially set to 10 days, 20 days and 30 days respectively, and the current density was

accordingly determined using Faraday's law, to be 0.45 mA/cm^2, 0.90 mA/cm^2, and 1.4 mA/cm^2 for the 8mm, 16mm, and 25mm steel specimens, respectively. Considering the potential loss of current during the electrification process, a reference steel bar was added in each diameter group. The reference bar was extracted from concrete after corroding for exactly 10 days to examine the actual corrosion level as measured by the mass loss rate μ_{mass}, which was determined by:

$$\mu_{mass} = \frac{m_0 - m_{cor}}{(l_{cor} / l_{total})m_0} \tag{1}$$

where m_0 and m_{cor} denote the mass of the rebar before and after corrosion over the length of l_{total}, respectively. l_{total} is the total length of the steel bar, which is 400mm. l_{cor} represents the length of the corroded section of the rebar. Considering that the corrosion length of each rebar may not be exactly the same, for simplicity a standardized value of 200mm is adopted here. By comparing the result with the target corrosion level (10%) and observe the difference, the actual electrified times for all specimens were adjusted by extrapolation.

After the required electrified times, the RC specimens were forced to break and the corroded bars were carefully extracted from the concrete. The extracted bars were then cleaned with an acid solution following the standard requirements [40]. After the corroded bars were completely dry, the weight of each corroded bar was weighted and μ_{mass} was determined accordingly. The results of corroded bars are listed in columns 2-6 in Table 2. All the corroded bars were then stored in a closed container filled with carbon dioxide to prevent secondary corrosion before mechanical testing.

In the process of electrified corrosion, the RC specimens cracked due to the expansion of corrosion products. The NaCl solution infiltrated into the concrete through the corrosion-induced cracks, and even some mixture liquid exuded from the top surface of the RC specimens, as can be seen in Fig. 1(c). As a result, a current circuit with lower resistance was formed between the ends of the corrosion region and the NaCl solution, and this accelerated the localised corrosion of the reinforcement, leading to a typical corrosion pit, as shown in Fig. 2. Similar phenomena have been observed in other experiments [41- 43]. It should be noted that some localised corrosion pits with the above-mentioned formation mechanism have discovered at some cracks in actual structures under the coupling effect of load and chloride corrosion [1, 32].
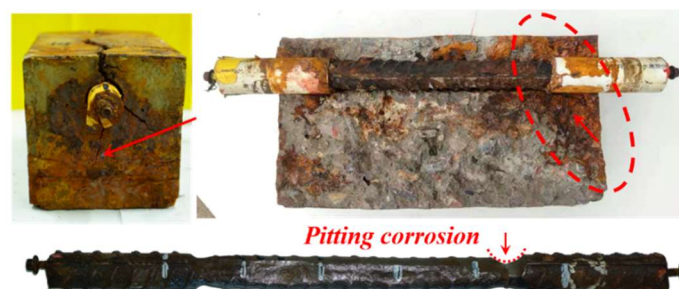

Fig. 2. The corroded specimens and the phenomenon of pitting corrosion.

Table 2. Details of corroded steel bars.

Specimens	m_0(g)	m_{cor}(g)	μ_t	Corrosion time/day	μ_{mass}	μ_{area}	μ_{max}
25-A1	1476.5	1396.4	10%	12.5	10.90%	9.98%	26.20%
25-A2	1476.5	1410.8	10%	12.5	8.90%	9.23%	32.20%
25-A3	1476.5	1395.6	10%	12.5	11.00%	9.97%	25.90%
25-B1	1476.5	1329.6	20%	25	19.90%	20.43%	45.00%
25-B2	1476.5	1304.1	20%	25	23.40%	23.75%	35.90%
25-B3	1476.5	1328.4	20%	25	20.10%	21.20%	46.40%
25-C1	1476.5	1283.8	30%	37.5	26.10%	28.21%	48.60%
25-C2	1476.5	1252.4	30%	37.5	30.40%	30.68%	48.90%
25-C3	1476.5	1264.5	30%	37.5	28.7%	29.08%	48.80%
16-A1	625.3	594.4	10%	12.5	9.90%	8.06%	17.20%
16-A2	625.3	591.4	10%	12.5	10.80%	9.59%	15.00%
16-A3	625.3	593.8	10%	12.5	10.10%	6.17%	28.10%
16-B1	625.3	567.3	20%	25	18.50%	16.96%	40.00%
16-B2	625.3	575.1	20%	25	16.00%	15.67%	43.60%
16-B3	625.3	573	20%	25	16.70%	15.37%	51.00%
16-C1	625.3	528.9	30%	37.5	30.80%	29.84%	78.70%
16-C2	625.3	540.8	30%	37.5	27.00%	26.66%	49.60%
16-C3	625.3	535.4	30%	37.5	28.80%	26.61%	46.00%
8-A1	158.6	152.5	10%	12.5	7.70%	5.29%	8.80%
8-A2	158.6	152.2	10%	12.5	8.10%	5.83%	9.40%
8-A3	158.6	142.9	10%	12.5	19.70%	13.63%	40.20%
8-B1	158.6	141.4	20%	25	21.70%	21.10%	32.40%
8-B2	158.6	145.5	20%	25	16.50%	15.21%	29.40%
8-B3	158.6	147.2	20%	25	14.40%	13.85%	29.70%
8-C1	158.6	141.3	30%	37.5	21.80%	20.60%	37.70%
8-C2	158.6	139.6	30%	37.5	23.90%	22.46%	78.20%
8-C3	158.6	145.5	30%	37.5	16.50%	16.57%	37.70%

2.2 Non-uniform corrosion morphology characterisation with 3D scanning technique

Compared to conventional measurement methods, the 3D scanning technique has the advantages of high efficiency, high precision, and no damage to the surface of the object. It is appropriate for reconstructing the virtual model of a corroded bar. In this study, a hand-held 3D scanner (HandyScan 300 from Creaform) with a scanning accuracy of 0.02 mm was employed to capture the corrosion morphology of the steel bars. The overall scanning setup is shown in Fig. 3(a). The measured data can be acquired in real-time by Geomagic software.
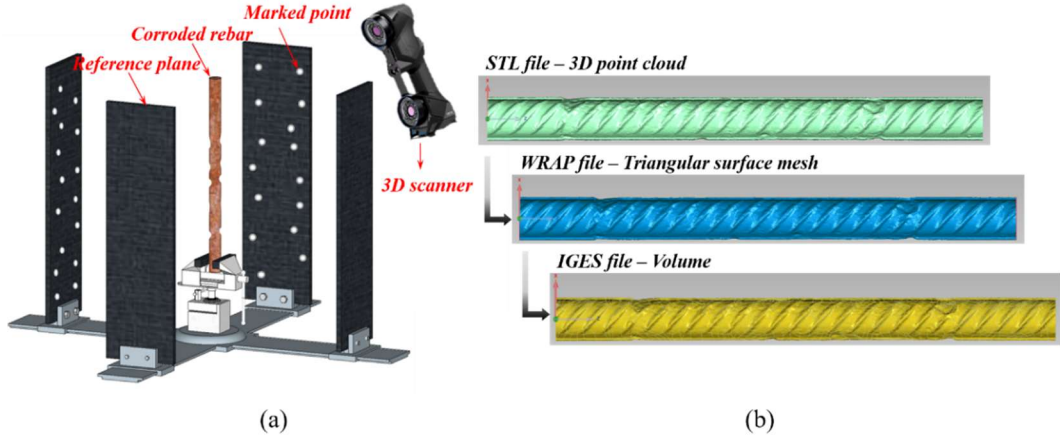
Fig. 3. (a) 3D scanning device for corroded steel bars (b) post-processing process.

After obtaining the point cloud file (i.e. STL file) containing the 3D spatial coordinate information of the corroded bars, a series of operations were still required, as shown in Fig. 3 (b), to obtain the cross-sectional areas data of the corroded bars. Considering the need for a reliable description of corrosion morphology and the requirement for sample size in statistical analysis, finally the residual cross-sectional areas of the corroded bars were extracted at 1mm intervals on the 3D model by Pro/Engineer software. The same interval was also used in other studies [18, 28, 38]. The distributions of residual cross-sectional areas for all corroded bars are shown in Fig. 4.

From the 3D scanning results, almost all the bars exhibited a significant pitting corrosion pattern, except for 8A1 and 8A2. For the 16mm and 25mm diameter bars, the corrosion pits were mainly located at the ends of the corroded zone, whereas for the 8mm diameter bars, the pits were distributed more randomly along the entire corrosion zone. It was evident that the actual corroded length was slightly larger than 200mm, so the mass loss rate μ_{mass} determined by a uniform length of 200mm is generally greater than the average sectional area loss rate μ_{area}, as shown in Table 2, where μ_{area} is determined by:

$$\mu_{area} = 1 - \frac{\sum_{i=1}^{n_{lcor}} A_{cor}(i)}{A_{0ave} \cdot n_{lcor}} \qquad (2)$$

where $A_{cor}(i)$ is the residual sectional area of the corroded bar at segment i; n_{lcor} is the total number of segment along the actual corroded length l_{cor}, taking the length where the sectional area on the corroded bar is less than the minimum sectional area of the original bar; A_{0ave} is the average cross-sectional area of the original bar. As corroded bars usually rupture in the section with the greatest loss of section during the tensile process, it is desirable to determine the maximum sectional area loss rate μ_{max} for each bar:

$$\mu_{max} = 1 - \frac{\min(A_{cor}(i))}{A_{0ave}} \tag{3}$$

The μ_{area} and μ_{max} of all corroded bars are presented in columns 7-8 in Table 2. Noting that 3D scanning has been extensively applied to the characterisation of corroded morphology and that its accuracy and reliability have been recognized by previous studies [18, 24, 27, 28], μ_{area} is adopted as the average corrosion loss rate μ_{ave} of the corroded bars in the subsequent sections of this paper.
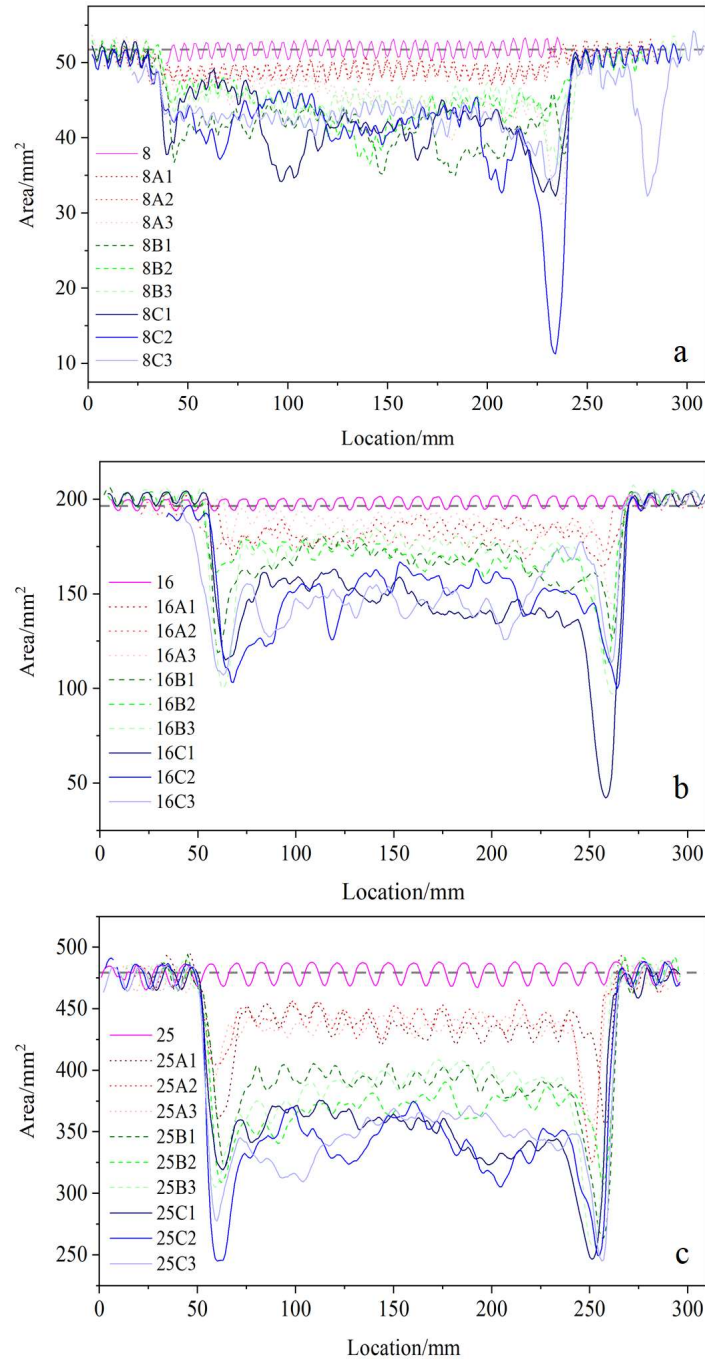

Fig. 4. Distribution of residual cross-sectional areas of (a) 8mm (b) 16mm (c) 25mm corroded bars along the longitudinal direction.

In order to quantitatively compare the corrosion morphology of corroded bars prepared by different studies [1, 24, 29], the correspondences between μ_{ave} and μ_{max} for corroded specimens are plotted in Fig. 5. The reference line (in blue colour) represents the ideal condition of perfect uniform corrosion, i.e. the maximum corrosion rate is equal to the average corrosion rate. In contrast, the data from a total of 14 corroded bars collected from 7 RC beams exposed to the marine environment under sustained load for 1.6 years to 28 years [1], plotted with "*" symbol and the corresponding regression relationship plotted in brown dash line, appear to represent a potential upper bound for the degree of non-uniform corrosion that could occur in actual structures. The data from present study and two other previous studies [24, 29] all fall within the above upper and lower bounds. It can therefore be argued that the degree of non-uniformity of the corroded specimens produced using laboratory accelerated corrosion with impressed current is within a realistic range.

It is worth noting that there is a lack of generally recognised criteria in the literature for classifying the degree of non-uniform corrosion. Since the regression relationship between μ_{ave} and μ_{max} for corroded bars provides a quantitative measure of the ratio between the maximum and average area loss for corroded bars at different corrosion levels, it could serve as a rational indicator to identify the degree of non-uniform corrosion. Establishing the correspondence between such a corrosion indicator and the erosion environment, as will be discussed later, could assist engineers in selecting a reasonable degradation model for evaluating the residual mechanical properties of bars in practice.
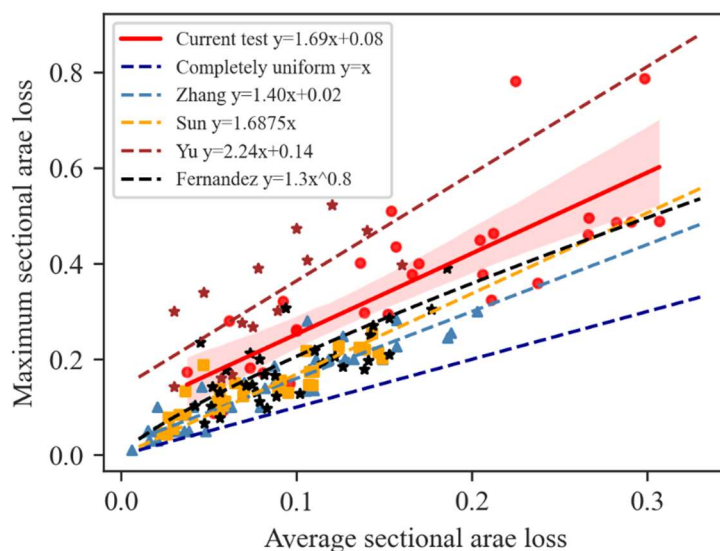

Fig. 5. Relationship between the average sectional area loss rate and the maximum sectional area loss rate.

2.3 Tensile testing and results

Monotonic uniaxial tensile tests were carried out on all corroded bars in accordance with the standard procedure [44]. A 100-ton universal testing machine was used in the test, and the load was applied under displacement control. The loading rate in the elastic

stage was set as 0.5 mm/min and then adjusted to 2 mm/min with the development of plastic deformation of steel bars. The force and total displacement applied by the testing machine were recorded. Considering that the traditional extensometer with fixed gauge length can only reflect the elongation of corroded bars at a specific distance and it needs to be removed before the specimen reaching the ultimate stage, this study adopted DIC technology to measure the entire deformation field of corroded bars. The overall loading and testing setup is shown in Fig. 6.

The DIC system used in this study consists of a pair of binocular stereo-vision cameras and post-processing software. The system captures the position information by two cameras simultanuously at the same acquisition frequency (1Hz in this study), and distinguishes the 3D coordinates of the point in the predefined coordinate system established by a priori calibration procedure for cameras. To improve the accuracy and efficiency of data acquisition, a layer of speckle on the surface of the corroded bars should be sprayed to form a high-contrast random pattern before the test, as shown in Fig. 6(c). From the captured information the surface deformation of the measured specimen in the whole vision field can be identified. Fig. 6(d) shows a representative deformation field of the 25C2 corroded bar under the maximum load.
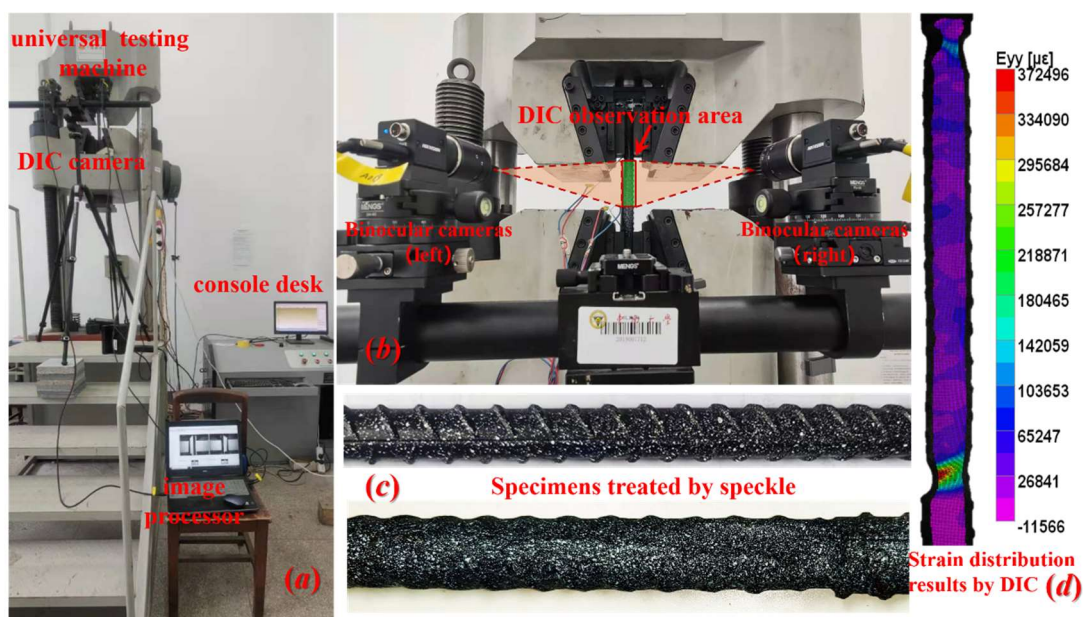

Fig. 6. Tensile testing and DIC set-up: (a) test system used for axial tensile tests (b) binocular stereo-vision camera (c) specimens treated by speckle (d) the strain distribution results by DIC.

For a verification of the accuracy of the DIC setup, a calibration test was performed on an HRB400 steel bar with a diameter of 8mm where three strain instruments, namely DIC, strain gauge and extensometer, were used simultaneously to measure the strain results. The stress-strain curves obtained from three measurements are shown in Fig. 7. It is noted that the nominal strain is determined by the ratio of the elongation over the extensometer gauge length to its original length. The stress-strain curves exhibit excellent agreement among the different measurement methods. However, due to the measurement range limitations, both strain gauges failed before

reaching a strain of 5%. The extensometer was removed from the specimen to avoid damage from premature fracture. Neither of the above two traditional methods could record the complete tensile process of the steel bar, while the DIC system captured not only the whole deformation process but also detailed distribution of deformation along the length of the specimen.

After the tensile tests of all corroded bars were completed, the DIC post-processing software was employed to calculate the deformation field. The strain results are determined with a uniform gauge length of 210mm, and the nominal stress of the corroded rebar is calculated with the average cross-section area of the original bar to enable easy comparison.
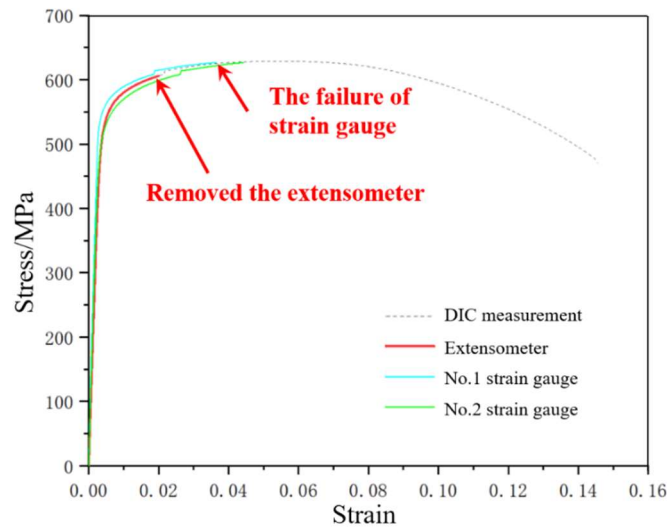

Fig. 7. Comparison of stress-strain curves from three measurements.

Fig. 8 shows the stress-strain curves of corroded rebar specimens for the three diameter groups, respectively. As the loading became unstable after the occurrence of necking during the test, the results are shown up to the end of the hardening stage for all bars. The ultimate strength and deformation refer to the force (stress) and the displacement (strain) of steel bars at the moment of the maximum load. It should be noted that the test data of specimen 16C2 is excluded from the subsequent mechanical property analysis because of the abnormal results, which were caused by some slip at the clamping end of the steel bar during the test. Three original bars for each diameter group are also tested, and the average results are used to represent the constitutive relationship of the original steel bars. Table 3 summarises the characteristic values of the mechanical properties of the original steel bars of the three diameters, respectively.

Table 3. Mechanical properties of original steel bars.

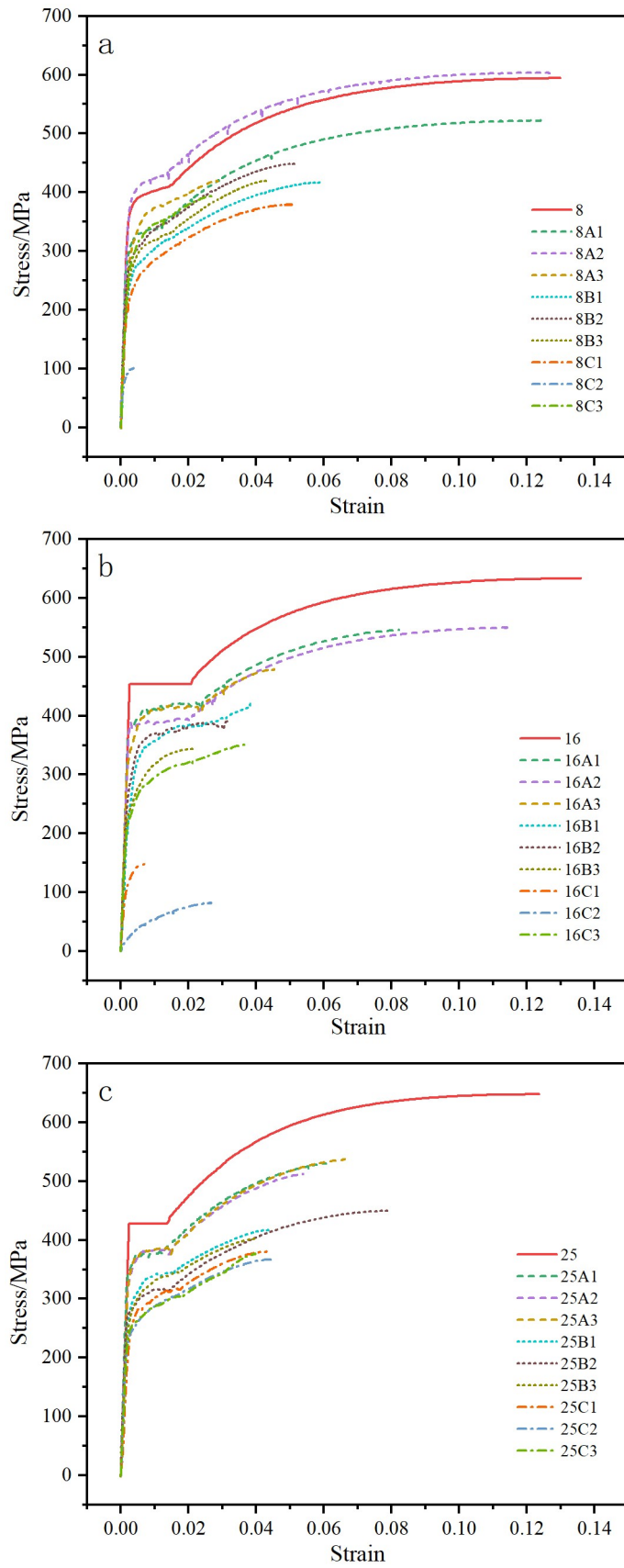| Diameter /mm	Yield stress /MPa	Yield strain /ε	Ultimate stress /MPa	Ultimate strain /ε
25	428.03	0.0023	647.64	0.1236
16	453.29	0.0025	633.71	0.1361
8	341.37	0.0022	578.38	0.1298

Fig. 8. Tensile test results for (a) 8mm (b) 16mm (c) 25mm corroded specimens.

3 Characterisation of non-uniform corrosion morphology

The morphological characteristics of corroded steel bars have been studied by many researchers using a statistical approach. However, due to the uncertainty of corrosion effects and the differences in the corrosion conditions, various probability distribution functions have been proposed by different studies, such as normal distribution [18], lognormal distribution [27], sinusoidal distribution [24], and Gumbel extreme value distribution [19, 42]. These probability distribution functions have not been classified into the applicable corrosion scenarios, and this leads to confusion in subsequent applications. Moreover, the above mentioned probabilistic functions are generally unsuitable for characterising the corrosion patterns with significant pitting due to the fact that the associated probability density curves are unimodal.
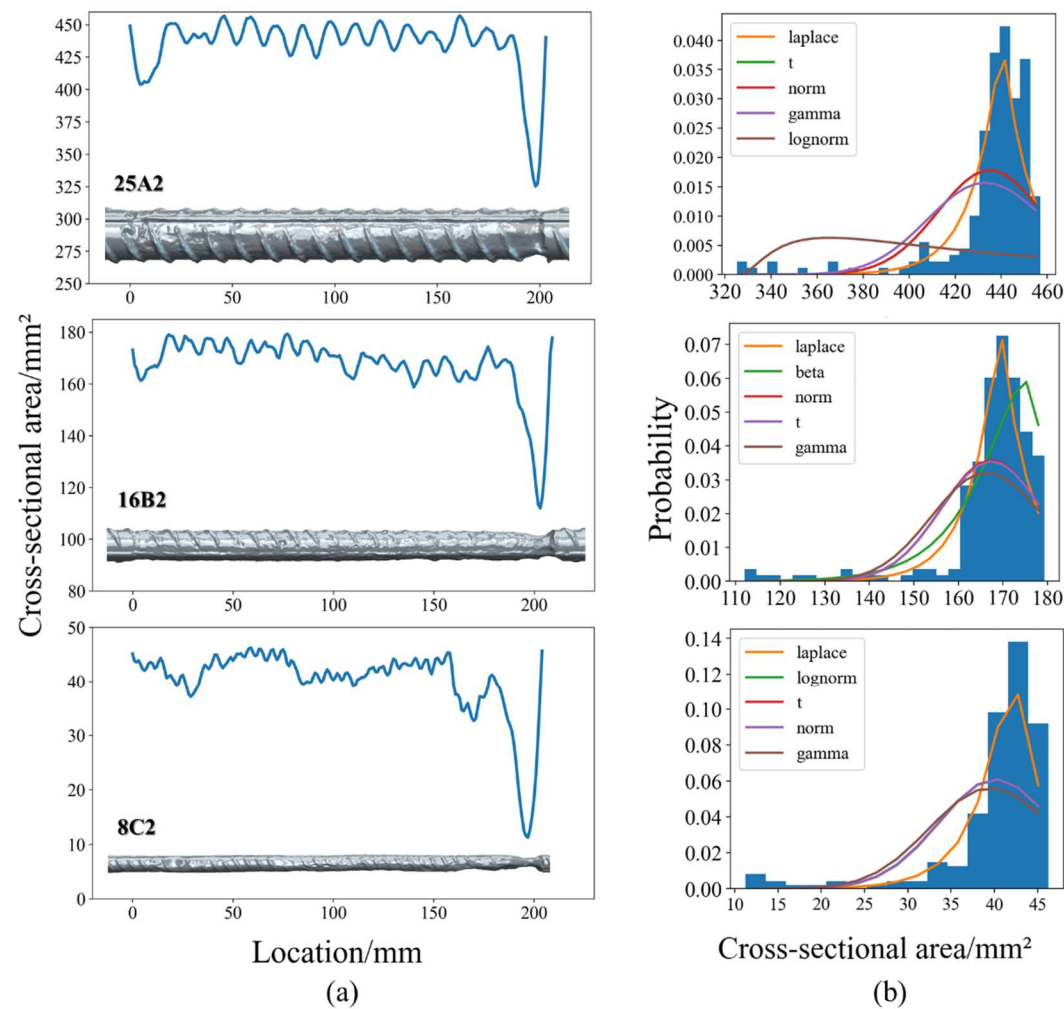
Fig. 9. The fitting analysis: (a) corrosion distribution along the rebar axis (b) histogram of residual cross-sectional area of steel bars and the corresponding fitting probability density curves.

In the present study ten common probability density functions were firstly tried to carry out the fitting analysis on representative pitting bars including specimens 25A2, 16B2 and 8C2, and five of these probabilistic functions with the smallest fitting errors were then selected, with the results plotted in Fig. 9. As the actual distributions are

14

dominated by the primary region around which most of the residual cross-section areas situate, the fitted distribution curves tend to be more biased towards the primary region of the sectional areas, whereas the region with larger corrosion pits (hence smaller cross-section area) is essentially omitted, as can be seen from Fig. 9 (b). However, in reality the mechanical properties of the corroded bars are generally governed by the minimum cross section, which means a realistic representation of the probability in the smaller residual cross section region is crucial. Based on this consideration, in this study we propose the adoption of a mixture probability model to depict the cross-section distribution characteristics of pitting steel bars.

3.1 Gaussian mixture model

The Gaussian mixture model (GMM) has been extensively used in the field of statistical analysis [45], which can give a more precise depiction of complicated data distribution. GMM is formed by a linear superposition of multiple Gaussian distributions, and can approximate any continuous distribution curve by employing a sufficient number of components and altering the coefficients (i.e., weight, mean and covariance) in the linear combination. The probability density function of GMM is generally written as:

$$f(x, w_k, \mu_k, \sigma_k) = \sum_{k=1}^{M} \frac{w_k}{\sigma_k \sqrt{2\pi}} \cdot e^{-\frac{(x-\mu_k)^2}{2\sigma_k^2}} \tag{4}$$

where x is a random variable; M is the number of components of GMM; μ_k and σ_k are the mean and standard deviation of the k-th Gaussian distribution, respectively; w_k is the weight coefficients of x up to the k-th Gaussian component, which represents the relative rate at which the observed sample belongs to the cluster of the k-th Gaussian component, and should satisfy the requirement that $0<w_k<1$, together with $w_1+w_2+…+w_M=1$. The expectation of GMM is:

$$P(x_i) = \sum_{k=1}^{M} w_k N\left(x_i; \mu_k; \sum_k\right) \tag{5}$$

where each Gaussian density $N(x_i; \mu_k; \Sigma_k)$ refers to a component of GMM and has its own mean μ_k and covariance Σ_k.

3.2 Parameter estimation for GMM

The parameters of a Gaussian mixture model are generally estimated using the expectation maximization algorithm (EM), i.e. for a given Gaussian mixture model, the objective is to obtain the value of the maximized likelihood function with respect to the parameters by iterative computation. The specific steps are as follows [45]：

   1) Initialize the mean μ_k, covariance Σ_k and weight coefficients w_k, and calculate the initial values of the log-likelihood function.

   2) E (expectation) step to calculate the responsibilities based on the current model parameters:

$$\gamma_{ij}^{(k)} = P\left(c_j \mid x_i\right) = \frac{w_j N(x_i \mid \mu_j, \Sigma_j)}{\sum_{k=1}^{M} M(x_i \mid \mu_k, \Sigma_k)} \tag{6}$$

3) M (maximization) step to re-estimate the parameters using the current responsibilities:

$$w_i^{new} = \frac{1}{N} \sum_{j=1}^{N} \gamma_{ij}^{(k)} \tag{7}$$

$$\mu_i^{new} = \frac{\sum_{j=1}^{N} \gamma_{ij}^{(k)} x_j}{\sum_{j=1}^{N} \gamma_{ij}^{(k)}} \tag{8}$$

$$\Sigma_i^{new} = \frac{\sum_{j=1}^{N} \gamma_{ij}^{(k)} \left(x_j - \mu_i^{new}\right)\left(x_j - \mu_i^{new}\right)^{T}}{\sum_{j=1}^{N} \gamma_{ij}^{(k)}} \tag{9}$$

where $\gamma_{ij}^{(k)}$ is the expectation generated by the k-th Gaussian component; w_i^{new}, μ_i^{new}, Σ_i^{new} are the corresponding parameter estimate, respectively.

4) Calculate the value of the logarithmic maximum likelihood function:

$$L(x) = \ln \prod_{i=1}^{N} P(x_i) = \sum_{i=1}^{N} \ln(\sum_{k=1}^{K} w_k N(x_k \mid \mu_k, \Sigma_k)) \tag{10}$$

Keep iterating steps 2) to 4) until the amount of change in the likelihood function is less than the error value or the number of iterations (the iteration error set in this study is 2E-16, and the maximum number of iterations is 500), the iteration ends, otherwise, return to step 2).

3.3 Evaluation for goodness-of-fit

In order to evaluate the goodness of fit between the determined GMM by the EM algorithm and the histogram of the cross-sectional distribution of pitting bars, it is crucial to select suitable evaluation metrics. Previous studies have routinely employed metrics such as coefficient of determination (R^2) and root mean square error (RMSE), and the essence of these metrics is to calculate the difference between the fitted and actual values. However, the actual values are dependent on the selection of the group spacing in the case of fitting data distributions. Different group spacing would directly affect the value of the probability density, and hence the results of the above error

metrics. For this reason, in this paper we adopt the Akaike Information Criterion (AIC) and the Bayesian Information Criterion (BIC) [46] in selecting the model and determining the model parameters. Both AIC and BIC are comprised of two parts, the first of which reflects the complexity of the model as a penalty term, and the second reflects the accuracy of the model, as expressed in the following:

$$AIC = 2m - 2L \tag{11}$$

$$BIC = m\ln(n) - 2L \tag{12}$$

where m represents the count of model parameters, n is the number of fitted data, and L is the value of the log-likelihood function of the model, which can be determined by Eq. 10.

In general, the higher the accuracy of the model fit, the smaller values of AIC and BIC correspondingly, and the model is better; however, when the values L of different models are close, the first part of Eqs. 11 and 12 would play a decisive role, thus the model is more simple, which is better. The applications of AIC and BIC can avoid the evaluation errors caused by different group spacing; besides that, BIC takes into account the influence of sample size in the penalty term, which can prevent the phenomenon of excessive model complexity arising from a high model accuracy.

As an exploration, different probability models, including GMMs with varying cluster numbers, are employed to fit the residual cross-section area distribution of 25A2, 16B2 and 8C2 bars. The corresponding values of AIC and BIC are determined and compared in Fig. 10 via bar charts, where $norm\_n$ represents the number of components in GMM. Compared to the unimodal probability distribution model, the fitting accuracy of the model is significantly improved with GMM when two or more components are involved, i.e. a significant decrease in the value of AIC. It can also be observed that introducing more components in the GMM results in an increased value of the BIC, whereas the value of AIC decreases only slightly, which means the fitting accuracy of the model is not improved substantially. Considering that a larger number of components in GMM leads to an increase in the complexity of the model, the GMM with two components appears to realize a good balance between the fitting accuracy and model complexity, and therefore can serve the best probability model for 25A2, 16B2 and 8C2 steel bars.

A comparison of the probability density curves of the two-component GMM with the histograms of the residual cross-section area of 25A2, 16B2 and 8C2 steel bars are shown in Fig. 11. The comparison results illustrate excellent agreement. In the two clusters of GMM, the two Gaussian components depict the cross-section area distribution of the uniform and pitting corroded sections of the bars, respectively.
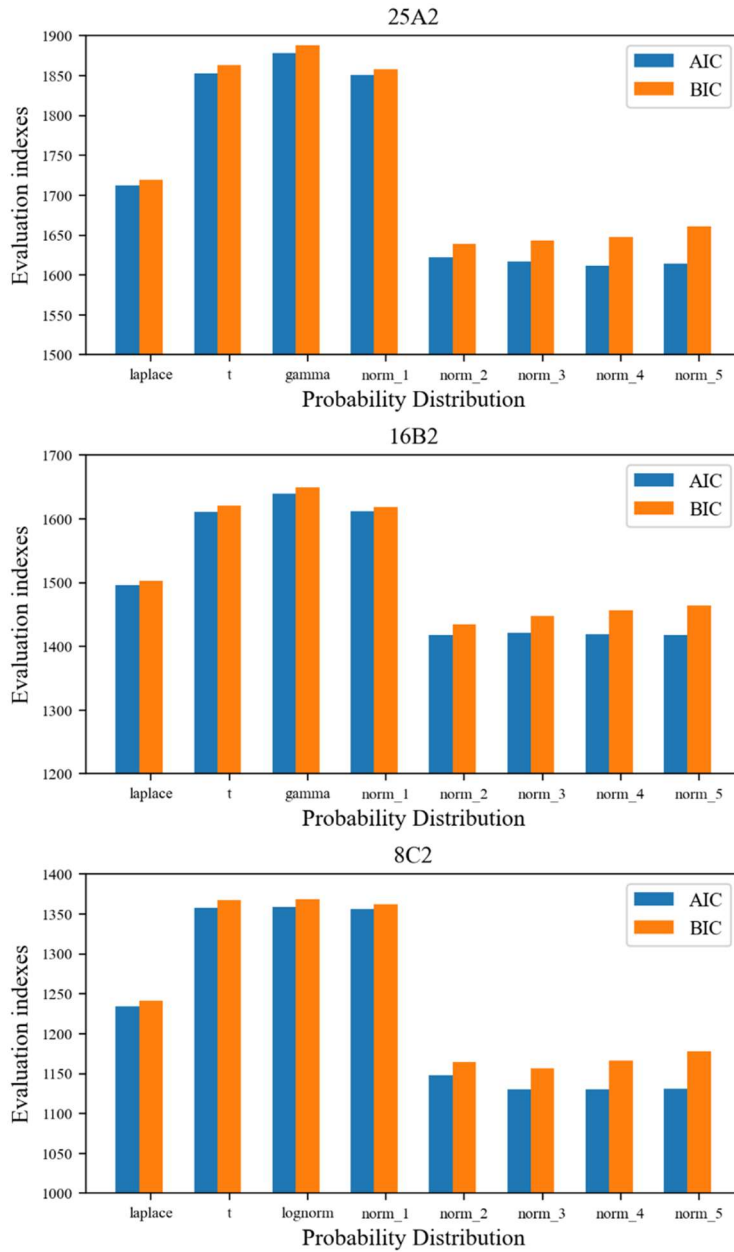
Fig. 10. The values of *AIC* and *BIC* for different probability models.
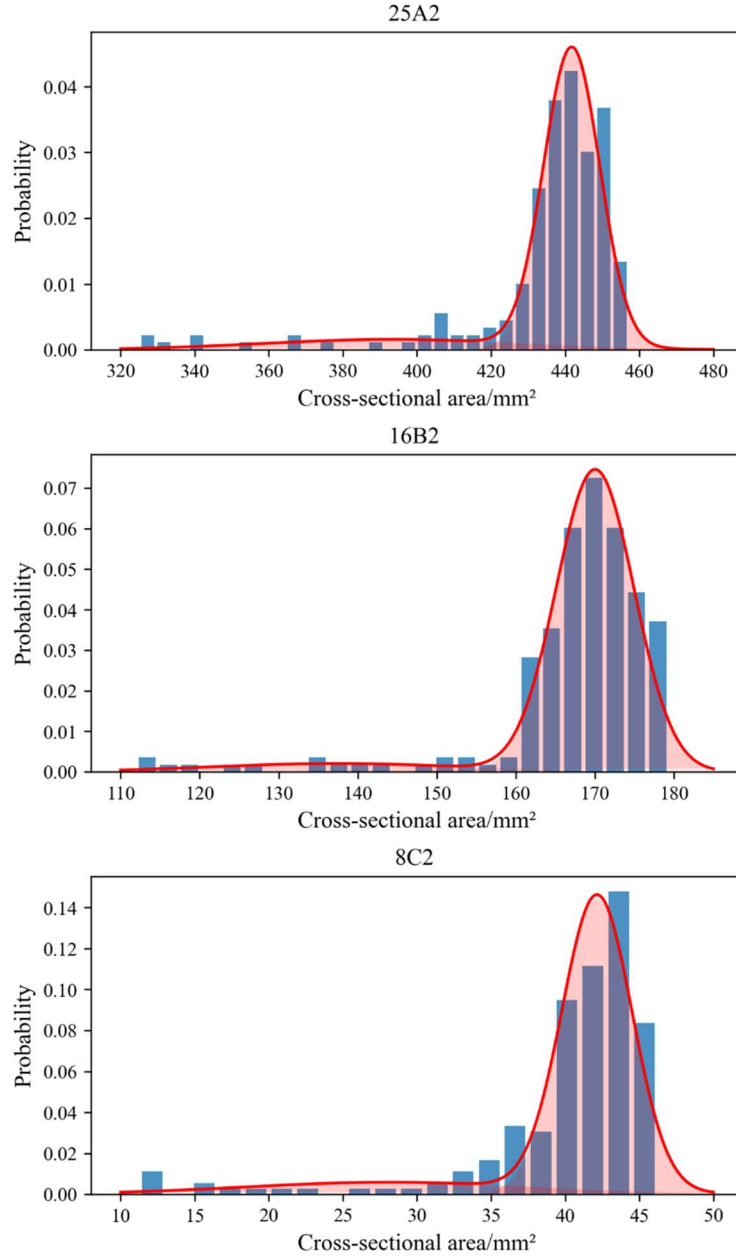
Fig. 11. Histograms of residual cross-sectional area of representative corroded bars and the corresponding fitting probability density curves with two-component GMM.

3.4 Probability model of residual cross-section distribution of pitting bars

From the experimental results, the residual cross-sectional areas of each corroded bar can be obtained through the process described in Section 2.3. These data are normalized (divided by the average cross-section area of the original steel bar) and subsequently treated as a random variable for cluster analysis based on the EM algorithm. A Gaussian mixture model with the optimum number of components is determined by comparing the *AIC* and *BIC* values. For example, GMM with different components is used to fit nine corroded bars in the 8mm diameter group, and the corresponding *AIC* and *BIC* values of the models are shown in Fig. 12. It is evident that when the number of

19

components is greater than 1, there is a significant decrease in the *AIC* and *BIC* values, i.e. a significant increase in model accuracy; when the number of components is greater than 2 or 3, the AIC values varies only slightly, and the BIC values increase rapidly due to the increase in parameters. Similar trends can be observed for 16mm as well as 25mm corroded bars.
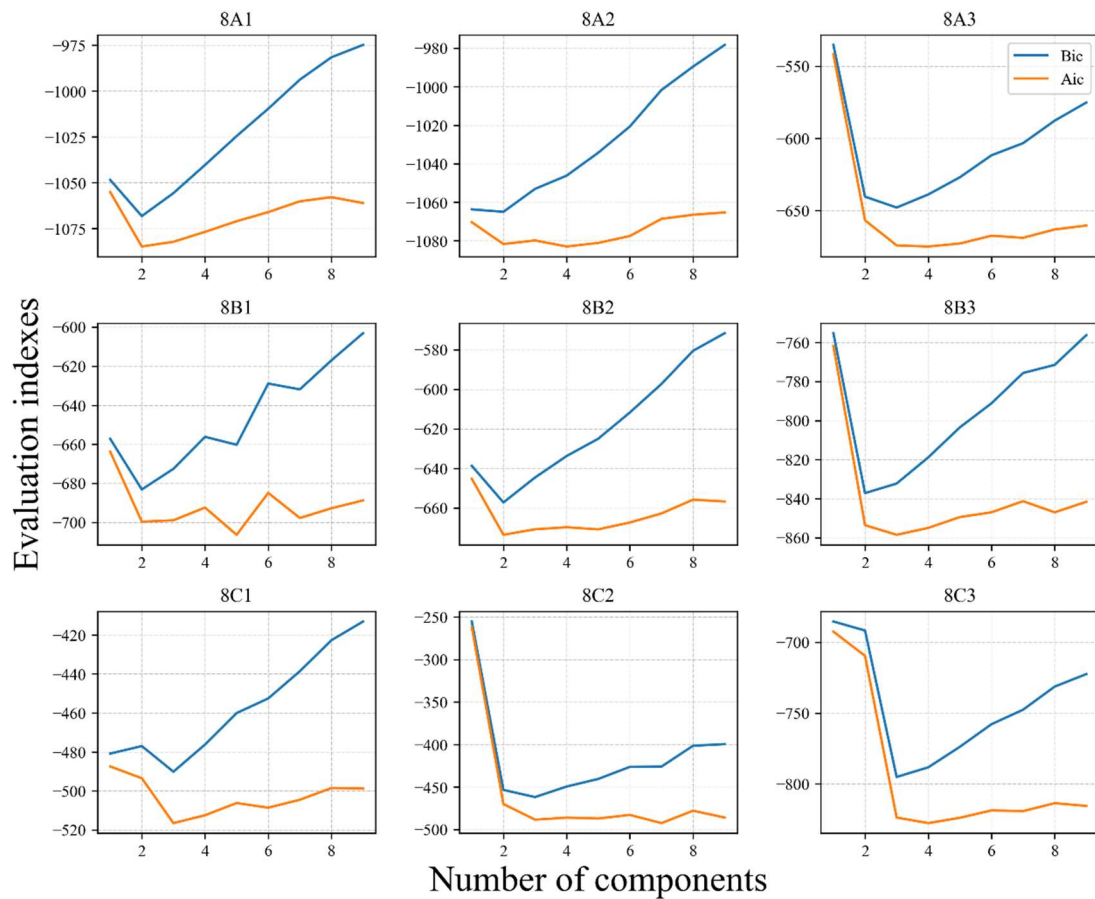

Fig. 12. The values of *AIC* and *BIC* for 8mm diameter corroded bars fitted by GMM with different number of components.

From the above analysis, it is clear that a GMM with two or three components is suitable for depicting the cross-sectional area distribution of most corroded steel bars in terms of the model accuracy. However, three additional parameters (i.e., weight coefficient, mean and variance) are required for each additional Gaussian component. Considering a good balance between the fitting accuracy and the complexity of the model, as well as the consistency of the subsequent analysis, a GMM with two components is employed to depict the cross-sectional area distributions of all corroded bars. In addition, the two-component GMM has a clearer physical meaning than the other models. The Gaussian component with a greater weight and a higher mean represents the cross-sectional distribution of the uniformly corroded portion in the steel bars, while another Gaussian component with a lower weight and mean reflects the cross-sectional distribution of the pitting corroded portion in the steel bars. This way, a direct link between the six parameters in the two-component GMM and the morphological characteristics of the corroded bars is established. The two weight

coefficients, w_1 and w_2, are related to the proportion of pitting segments among the overall length, while the two mean coefficients, m_1 and m_2, are related to μ_{ave} and μ_{max} respectively, and the two variance coefficients, v_1 and v_2 determine the specific shape of the distribution. The values of the parameters determined by the EM algorithm are presented in Table 4.

Table 4. The parameters of two-component GMM for corroded specimens.

Specimens	μ_{ave}	μ_{max}	w_1	m_1	v_1	w_2	m_2	v_2
25A1	0.0998	0.2618	0.9143	0.9111	-7.8530	0.0857	0.7838	-6.8365
25A2	0.0923	0.3215	0.8609	0.9218	-8.2930	0.1391	0.8206	-5.2349
25A3	0.0997	0.2590	0.8844	0.9115	-8.8924	0.1156	0.8143	-6.3211
25B1	0.2043	0.4501	0.8387	0.8171	-8.3171	0.1613	0.6848	-5.1830
25B2	0.2375	0.3586	0.7911	0.7765	-8.0214	0.2089	0.7095	-6.4995
25B3	0.2120	0.4644	0.7942	0.8142	-7.4363	0.2058	0.6870	-5.0568
25C1	0.2821	0.4858	0.9287	0.7298	-6.8483	0.0713	0.5620	-6.4718
25C2	0.3068	0.4885	0.8669	0.7120	-6.7305	0.1331	0.5708	-5.9603
25C3	0.2908	0.4884	0.7027	0.7333	-7.3852	0.2973	0.6522	-5.7156
16A1	0.0806	0.1717	0.6357	0.9331	-8.2475	0.3643	0.8956	-7.0414
16A2	0.0959	0.1504	0.5598	0.9133	-8.3721	0.4402	0.8969	-7.7535
16A3	0.0617	0.2813	0.9251	0.9489	-7.9876	0.0749	0.8081	-5.3940
16B1	0.1696	0.3997	0.8108	0.8482	-6.7604	0.1892	0.7542	-5.1097
16B2	0.1567	0.4355	0.9173	0.8569	-7.3917	0.0827	0.6926	-5.0515
16B3	0.1537	0.5100	0.8149	0.8895	-7.8063	0.1851	0.6561	-4.1709
16C1	0.2984	0.7873	0.9241	0.7304	-5.8242	0.0759	0.3508	-4.1661
16C2	0.2666	0.4961	0.7281	0.7758	-6.9097	0.2719	0.6197	-5.6797
16C3	0.2661	0.4604	0.5526	0.7622	-5.5392	0.4474	0.6989	-5.3220
8A1	0.0529	0.0883	0.5455	0.9610	-9.3490	0.4545	0.9303	-9.2456
8A2	0.0583	0.0943	0.5256	0.9559	-9.0172	0.4744	0.9259	-8.9347
8A3	0.1363	0.4024	0.9368	0.8759	-6.7388	0.0632	0.6820	-5.4162
8B1	0.2110	0.3238	0.6782	0.8149	-7.5211	0.3218	0.7345	-7.1031
8B2	0.1521	0.2941	0.6931	0.8701	-7.3319	0.3069	0.7978	-6.3549
8B3	0.1385	0.2968	0.9381	0.8682	-7.6827	0.0619	0.7597	-6.5802
8C1	0.2060	0.3769	0.7286	0.8249	-6.0758	0.2714	0.7110	-5.9396
8C2	0.2246	0.7824	0.8521	0.8149	-6.1831	0.1479	0.5478	-3.3356
8C3	0.1657	0.3776	0.9146	0.8450	-5.8655	0.0854	0.7195	-5.3489

Note: The parameters of v_1 and v_2 in the table are logarithmically processed values.

4 Prediction for the mechanical properties of pitting bars

Most previous studies have developed semi-empirical equations to estimate the deterioration degree of the mechanical properties of corroded bars. However, these results have significant drawbacks, as mentioned before. In this section, a simplified theoretical method is proposed for assessing the residual mechanical properties of corroded bars in conjunction with the study of the cross-sectional area distribution characteristics of pitting bars in Section 3.

4.1 Theoretical calculation method for the evaluation of the deformation capacity of corroded bars

Several investigations have reported that the influence of corrosion on steel bars can be regarded as the loss in cross-section only, without inducing a change in the material intrinsic properties [47, 48]. Therefore, the residual load bearing capacity of a corroded reinforcing bar depends mainly on its minimum remaining cross-sectional area, while the tensile deformation capacity need to be determined by the residual cross-sectional areas of the whole reinforcing bar [49]. A simplified theoretical method for calculating the deformation capacity of corroded bars is therefore proposed based on the above assumptions, and the specific steps are as follows:

(1) Determine the actual cross-sectional area of corroded bars at an appropriate interval, herein using 1 mm, and calculate the stress values for individual sections under the current tensile force at each loading step according to Eq. 13：

$$\sigma_{ij} = \frac{F_j}{A_i} \tag{13}$$

where F_j is the total tensile force on the steel bar at step j; A_i is the residual sectional area of the i-th section of the steel bar; σ_{ij} is the nominal stress produced by the external load F_j at the corresponding section. The maximum value of F_j is the maximum load value during the real tensile test of the corresponding corroded bar.

(2) The intrinsic mechanical properties of the corroded bars are assumed to be unchanged. The strain value ε_i for the corresponding incremental segment i (of 1-mm length herein) is determined by the value of σ_{ij} obtained in step (1) and the stress-strain relationship for the original steel bar. It should be noted that at the moment of maximum load, some regions of the corroded bar, especially those near the corrosion pits, may already exhibit the phenomenon of necking. This means the actual stress σ_{ij} calculated in some small segments may be greater than the ultimate stress f_u defined in the stress-strain curve of the original bar. Considering the uncertainties in the cross-section area around a necking location and for a conservative consideration, when $\sigma_{ij} > f_u$, the strain value ε_{ij} is taken equal to the ultimate strain ε_u of the original steel bar.

(3) Calculate the elongation of each incremental segment under each tensile load according to Eq. 14, and the total elongation Δ_{total} of the corroded bar by accumulating the deformation values of all segments, as

$$\triangle_{total} = \sum \delta_i = \sum_{i=1}^{l_{cor}} l_i \cdot \varepsilon_i \tag{14}$$

Thus the load-displacement curve of the corroded rebar is established.

Three representative corroded bars (25C2, 16A1, 8B2) are taken from all bar specimens to illustrate the analysis process and results. The load-displacement curves for these corroded bars are computed according to the above procedure and then compared with the direct results from the tensile tests. The computed load is divided

into 300 steps from 0kN to the maximum test load. The load-displacement curves are converted into nominal stress-strain curves to facilitate comparison across specimens of different diameters. The nominal stress of the corroded bar is calculated by dividing the tensile load by the average cross-sectional area of the original bar, and the nominal strain is calculated by dividing the displacement by the gauge length which is taken as 210 mm.

The comparison results are shown in Fig. 13. The curves obtained by the theoretical calculation method are drawn with dashed lines, and the stress-strain curves from the tests are drawn with solid lines. It can be seen that the shapes of the computed curves match very well with the test curves, and yield and ultimate stages of the computed results also fit the direct test results with good accuracy. The computed ultimate deformation capacity of the bars appears to be lower than the actual test values. Although the difference is not significant from the view point that the ultimate deformation could vary quite markedly even between different specimens of the same original bars, the fact that the computed deformation always appears to be lower is something worth investigating. In what follows, the strain distribution data along the length of the corroded bar at the moment of the maximum load is extracted to analyse the reason for this situation.
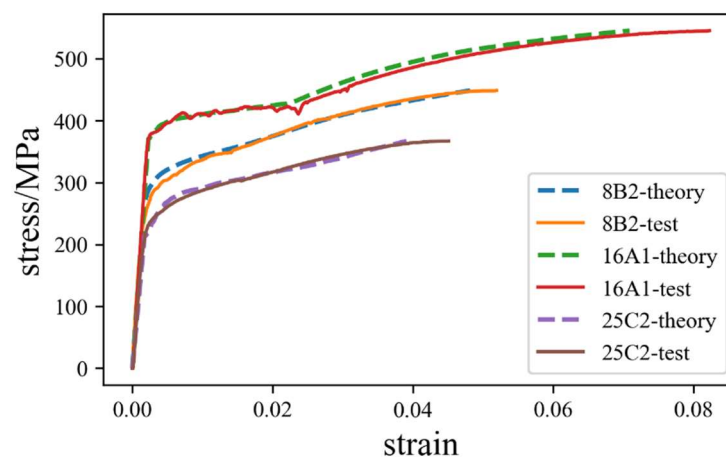

Fig. 13. Comparison between the test results of corroded bars and theoretical results.

Fig. 14 shows the distribution of (real) strains along the length of the bar specimens, in which extracted strain distributions from the actual tensile tests by the DIC technique are shown in orange curves, while the computed strain distributions by the theoretical method are shown in blue curves. In addition, the distributions of the residual cross-sectional areas of the corroded bars are also included, shown in grey curves, for an observation. It is apparent that the strain distribution determined using the theoretical calculation method is in general agreement with the actual test curves. It can be noted that in the vicinity of the critical section, i.e., the smallest cross-sectional area, the computed strain has a cap due to the imposed limit of stress, σ_{imax}, at the ultimate stress f_u of the original bar. In the actual test, the local necking of the steel bar at the critical pitting locations resulted in a higher stress and higher strain. Zhou et al. [43] determined the precise strain values along the corrosion pits using numerical simulation. But for

plastic materials, especially steel bars, it is generally known that after reaching the necking stage, small cavities are formed inside the bars due to microscopic defects within the material; as the deformation proceeds, these microscopic holes expand, gather and merge to form an elliptical crack, which eventually spreads to the entire neck resulting in the fracture of the bar [50]. Indeed, the state of the reinforcement at this stage is unstable, and fracture may occur at any time. From this point of view, it is not considered to be meaningful to attempt to fit the extra strains arising from the occurrence of necking. Nevertheless, the above analysis provides a further assurance that the computed stress-strain results essentially fits very well the actual test results even in terms of the nominal ultimate strain.
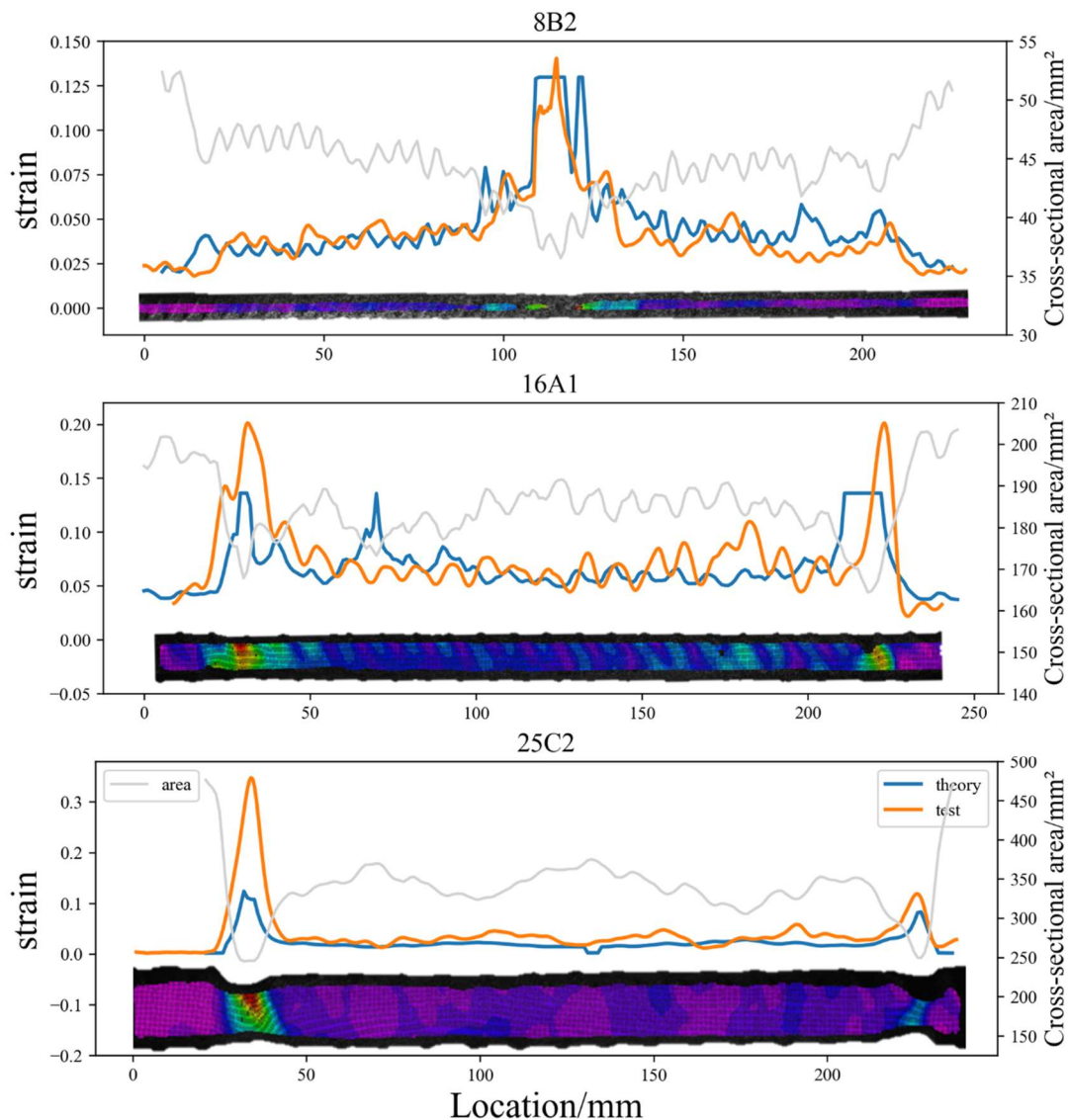

Fig. 14. Axial strain distribution for three corroded bars at the moment of ultimate load.

4.2 GMM-based evaluation method for the mechanical properties of pitting bars

From the analyses in the previous section, the residual mechanical properties of the corroded bars depend primarily on the stress-strain relationship of the original bars and the specific value of the residual cross-sectional areas after corrosion, while the

sequence of the arrangement of the cross-sectional area does not have a considerable effect on the ultimate deformation capacity of the corroded bars. Therefore, following a satisfactory verification of the above theoretical calculation method for the residual cross section area by the DIC technique, this method is further developed for the assessment of the mechanical properties of corroded bars by statistical means to reduce the dependence on actual morphological data.

4.2.1 Assessment for the ultimate load capacity

An accurate assessment of the ultimate load capacity of pitting bars is a fundamental prerequisite for further predicting their deformation behaviour. For pitting steel bars, at the moment of maximum tensile external force, a portion of the bar has prematurely reached the necking stage in the vicinity of a localised corrosion pit. The real axial stress at the critical section is strengthened under a multi-axial stress condition. Consequently, when the stress in the section is determined by adopting the minimum residual cross-sectional area, a slightly increasing tendency is observed at the moment of maximum loading of the pitting bars compared with the corresponding original bars [17-19].

As the steel bar reaches the plastic hardening stage after yielding, even a minor stress enhancement can generate a large increment in the overall deformation or nominal strain. Thus the ultimate-stress-strengthening effect of pitting bars cannot be disregarded. The ultimate-stress-strengthening coefficient k for corroded bars is defined according to Eq. 15:

$$k = [\frac{T_{max}}{(1-\mu_{max})A_{0ave}}] / f_{u0} \tag{15}$$

where T_{max} is the maximum load value in the tensile test; f_{u0} is the ultimate stress value of the original steel bar. The values of k for the pitting bars prepared in this study are calculated based on Eq. 15 and presented in Table 5.

Table 5. The ultimate-stress-strengthening coefficient k for corroded bars.

Diameter	A1	A2	A3	B1	B2	B3	C1	C2	C3	Mean value	St-dev
25mm	1.13	1.19	1.15	1.20	1.11	1.19	1.17	1.13	1.16	1.16	0.03
16mm	1.05	1.04	1.07	1.13	1.11	1.12	1.11	NA	1.04	1.08	0.03
8mm	0.96	1.12	1.18	1.04	1.07	1.00	1.02	NA	1.06	1.06	0.06
Mean value		1.10			1.11			1.10		1.10	0.06
St-dev		0.07			0.06			0.05			

In Table 5, the specimens are classified in terms of diameter and corrosion rate μ_t. The mean value of k obtained from the different corrosion rates is almost unchanged and remains around 1.1, indicating that there is no significant correlation between k and the corrosion rate. In contrast, when the test data is classified according to diameter, the mean value of k increases from 1.06 to 1.16 with increasing diameter of bars, and the standard deviation (St-dev) is lower compared to the results classified by μ_t. These results demonstrate that for larger diameter bars, the multi-axial stress condition tends

25

to get more enhanced, and as a result the overall tensile deformation capacity of the corroded bar becomes more pronounced.

A regression between the mean values of k and the bar diameter curve is fitted which can be expressed by:

$$k = 0.008 \cdot D + 0.965 \tag{16}$$

Subsequently, the GMM is considered for generating the cross-sectional information for pitting bars in the absence of the actual test values, and from there the minimum cross-sectional area $\hat{A}_{min}$ is picked. The ultimate load capacity F_{max} of the pitting bars can then be calculated following Eq.17 and Table 5:

$$F_{\max} = k \cdot \hat{A}_{\min} \cdot f_{u0} \tag{17}$$

Take the real test value of the pitting bars as the x-coordinate and the predicted value as the y-coordinate and plot a scatter diagram to observe the comparison. Fig. 15 (a) and (b) show the predictions without and with the ultimate-stress-strengthening coefficient k, respectively. It can be seen that the ultimate load capacity of 16mm and 25mm pitting bars is notably underestimated when the ultimate-stress-strengthening effect is not taken into account. After multiplying the corresponding mean value of k determined by different diameters of steel bars, the predictions are significantly improved and all scatter dots are closer to the reference line $y = x$. These demonstrate, on the one hand, the necessity to consider stress strengthening effect and, on the other hand, the reliability of the values of k obtained according to the diameter classification in Table 5.
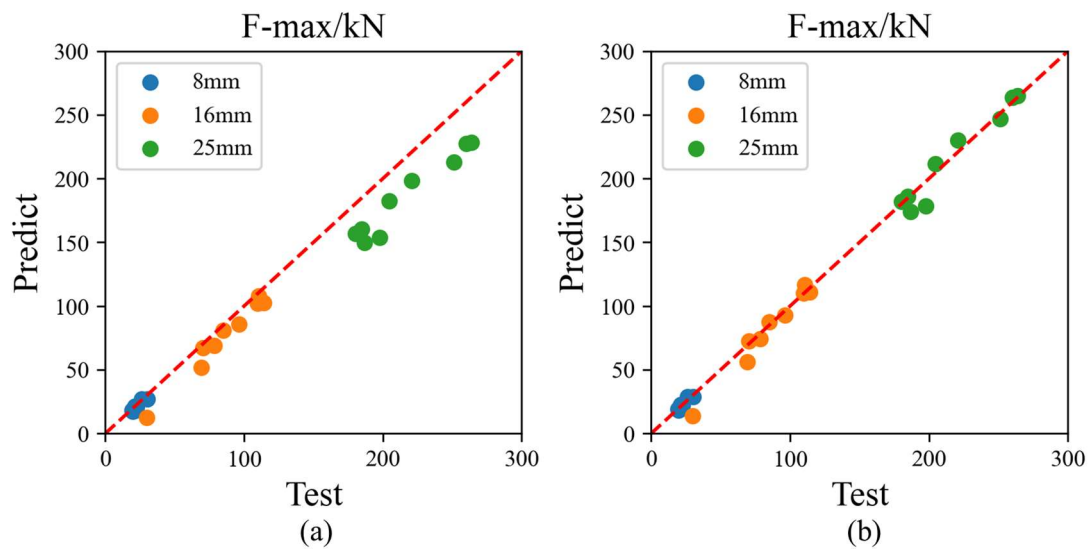

Fig. 15. Comparison between the test ultimate strengths and the predicted values (a) without and (b) with the consideration of the ultimate-stress-strengthening effect.

4.2.2 Assessment for the deformation capacity with different gauge lengths

For the analysis of the plastic deformation capacity of RC members involving corroded bars, an accurate calculation of the ultimate deformation capacity of the corroded bars

across the plastic region is a key. As the size (length) of the plastic region can vary in different applications, it is important that any dependency of the normalised deformation capacity (nominal strain) of corroded bars to the gauge length, over which the nominal strain is evaluated, be clearly established.

From the results in previous sections, the strain distribution along the length of pitting bars under tension is not uniform, therefore the nominal ultimate strain is dependent upon the gauge length. In this section, the elongation of the pitting bars is derived by employing the GMM fitted in Section 3.4 to generate a set of sectional areas for the corroded bars. Three gauge lengths, i.e., 50mm, 100mm and 210mm, are set to demonstrate the correlation of the normalised ultimate strain with the gauge length.
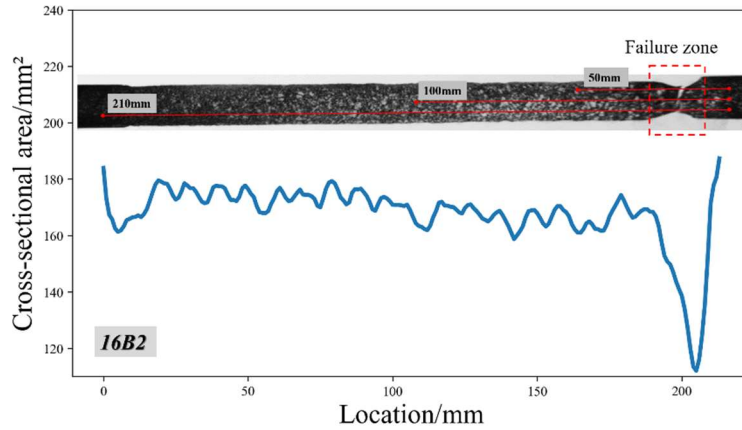

Fig. 16. Setup of the DIC virtual extensometer.

It is noted that the clamping range of the extensometer in the tensile test is required to cross the failure zone of the steel bar [44]. Therefore the virtual extensometers with three gauge lengths are set up in the DIC post-processing software, the exact locations of which are shown in Fig. 16. As the gauge length decreased, massive uniformly corroded pieces of reinforcement are excluded, while pitting pieces of reinforcement are still retained. The proportion of the pitting segment changes significantly within the clamping range of the 50mm and 100mm virtual extensometers. The parameters w_1 and w_2 of the corresponding GMM in Table 4 were thus corrected according to Eq. 18：

$$\begin{cases} w_2' = \dfrac{l_{cor} \cdot w_2}{l_{gauge}} \\ w_1' = 1 - w_2' \end{cases} \tag{18}$$

where l_{cor} is the corrosion length of the corroded bars, which is taken as 210mm uniformly; l_{gauge} is the gauge length, and w_1' and w_2' are the corrected weight coefficients, respectively.

The cross-sectional data with 50, 100 and 210 are randomly generated by python, in accordance with the method in section 4.2.1 to determine the ultimate load and following the steps in section 4.1 to evaluate the ultimate deformation of the pitting bars over the whole gauge length. Similarly, the comparison results are plotted in scatter diagrams and shown in Fig. 17, where GL indicates Gauge length. The elongations of

the pitting bars are well predicted by the theoretical method, regardless of whether the gauge length is 50 mm, 100 mm or 210 mm. The predicted values for most of the bars are slightly smaller than the test values for the reasons analysed in section 4.1. The contrast results demonstrate that the theoretical method developed in this section is capable of assessing the ultimate deformation capacity of corroded bars with arbitrary lengths. On the other hand, it also indicates that the randomly generated pitting bar cross-section data by GMM is close to the original cross-section data, and the GMM can well characterise the probability distribution of the cross-sectional areas of pitting bars.
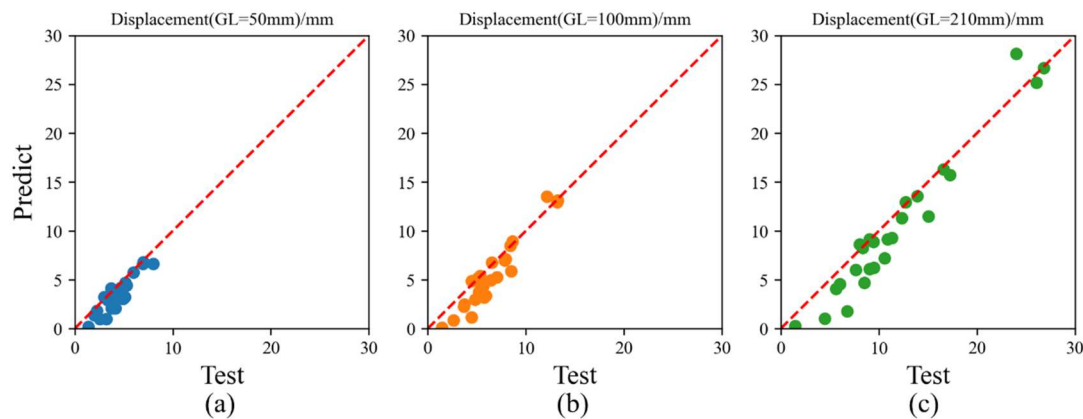

Fig. 17. Comparison between the test ultimate elongations and the predicted values with (a) 50mm (b) 100mm (c) 210mm gauge length.

4.2.3 Comparison with available prediction models

For a comparison with other prediction models available in the literature, Table 6 summarises two models proposed by other researchers. In the table, α_{uc} and $\alpha_{\varepsilon c}$ denote the ratio of the nominal ultimate strength and nominal ultimate strain of the corroded bar to the corresponding properties of the original bar, respectively. μ_{ave} and μ_{max} bear the same meaning as defined in this paper and they represent the overall corrosion and pitting levels.

Table 6. Summary of two other prediction models of corroded bars.

Authors	Diameter/mm	Gauge length/mm	α_{uc}	$\alpha_{\varepsilon c}$
Zhang et al. [23]	6/8/10/12 16/ 25	50	$\alpha_{uc} = 1 - 1.201\mu_{ave}$	$\alpha_{\varepsilon c} = \exp(-3.789\mu_{ave})$
Zhang et al. [24]	8/10/12 14/16	5*D	$\alpha_{uc} = 1 - 1.405\mu_{ave}$	$\alpha_{\varepsilon c} = -0.287 + 1.251\exp(-3.492\mu_{ave})$ $\alpha_{\varepsilon c} = -0.046 + 1.032\exp(-3.673\mu_{max})$

Using these models, the ultimate loads and the tensile deformation corresponding to 50 mm, 100 mm and 210 mm gauge lengths are calculated for the pitting bars prepared in this study. All the results are shown in Fig. 18, where the predictions obtained from the theoretical method of this study (referred to as the GMM method) are shown in blue solid circle symbols, while the predictions determined from the other models are shown in different coloured hollow circle symbols. It can be clearly

observed that the ultimate loads predicted by the GMM method are notably closer to the actual test values comparing with the results determined by the other models, although all results appear to be consistent with the test results in terms of the trend. When it comes to the prediction of the ultimate deformation capacity of the steel bars (Fig. 18 (b), (c) and (d)), however, the GMM method shows considerable improvement from the other models not only in terms of the trend but also the accuracy.
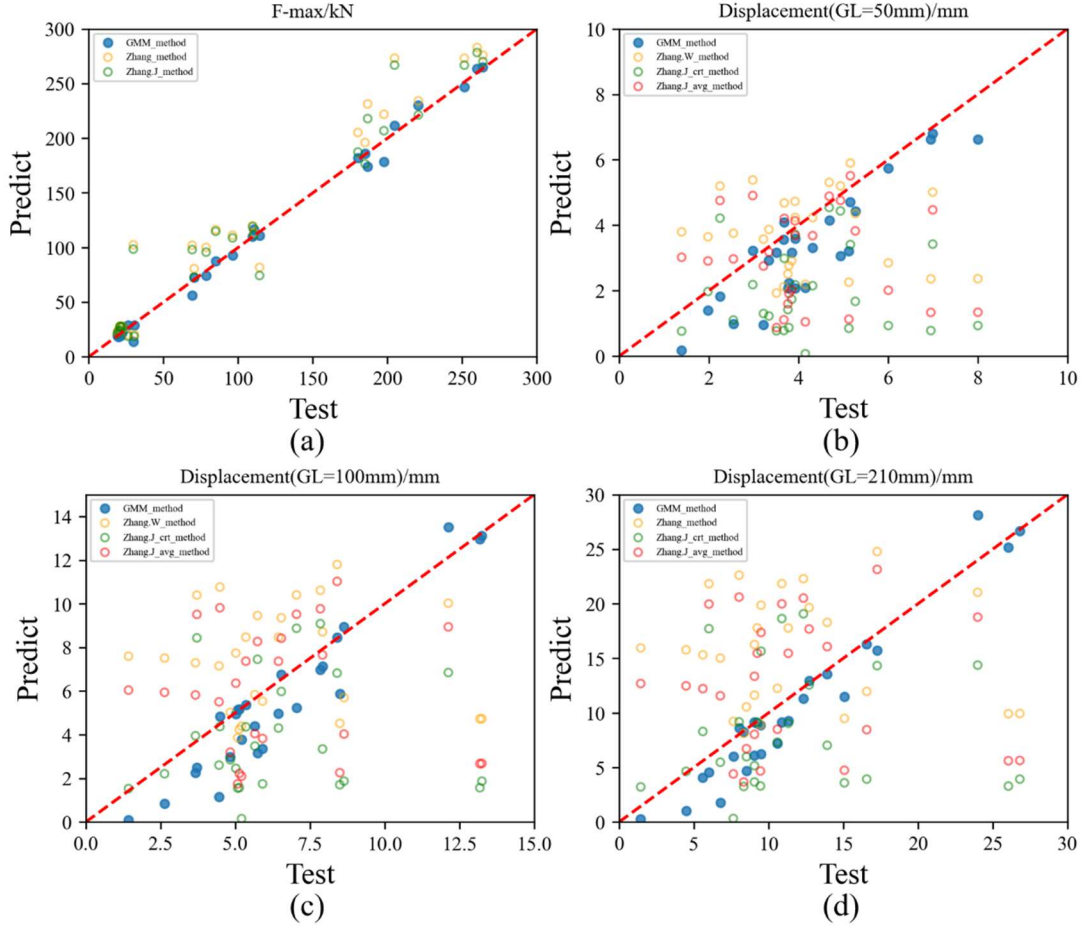

Fig. 18. Comparison between test and predicted values by different methods: ultimate load (a) and ultimate elongations with different gauge lengths (b) 50mm (c) 100mm (d) 210mm.

The prediction accuracy between different models is further examined using four error indices, namely Pearson correlation coefficient ($R_{pearson}$), root mean square error (RMSE), mean absolute percentage error (MAPE), and symmetric mean absolute percentage error (SMAPE), expressed as follows:

$$R_{pearson} = \frac{\text{cov}(\hat{Y}, Y)}{\sigma_{\hat{Y}} \cdot \sigma_Y} = \frac{E[(\hat{Y} - \mu_{\hat{Y}})(Y - \mu_Y)]}{\sigma_{\hat{Y}} \cdot \sigma_Y} \tag{19}$$

$$RMSE = \sqrt{\frac{1}{n} \sum_{i=1}^{n} (\hat{y}_i - y_i)^2} \tag{20}$$

$$MAPE = \frac{100\%}{n} \sum_{i=1}^{n} \left| \frac{\hat{y}_i - y_i}{y_i} \right| \tag{21}$$

$$SMAPE = \frac{100\%}{n} \sum_{i=1}^{n} \frac{|\hat{y}_i - y_i|}{(|\hat{y}_i| + |y_i|)/2} \tag{22}$$

where $\hat{y}_i$ is the predicted value and y_i is the corresponding test value. $R_{pearson}$ reflects the correlation between the predicted and tested values, and its value ranges between 1 and -1; A value closer to 1 means that the two data sets are positively correlated, closer to -1 means that they are negatively correlated, and closer to 0 means that they are not correlated. The other three metrics directly reflect the magnitude of the error between the predicted values and the actual values, with larger values indicating larger errors. The error results are compared in Table 7 and Table 8 for the ultimate stress and strain, respectively.

Table 7. Error between predicted and tested values of maximum load on pitting bars.

Method	$R_{pearson}$	RMSE/kN	MAPE/%	SMAPE/%
GMM-method	0.997	6.94	6.53	7.42
Zhang et al. [23]	0.975	27.0	28.8	22.3
Zhang et al. [24]	0.972	23.7	25.4	20.1

Table 8. Error between predicted and tested values of maximum elongations on pitting bars.

Method	Gauge length/mm	$R_{pearson}$	RMSE/mm	MAPE/%	SMAPE/%
GMM-method	50	0.902	1.16	26.4	34.9
	100	0.955	1.46	23.7	32.5
	210	0.973	2.27	21.9	29.5
Zhang et al. [23]	50	-0.129	2.11	43.9	42.9
	100	-0.0767	4.00	68.4	46.9
	210	-0.0750	9.21	113	57.0
Zhang et al. [24]-crt	50	0.0158	3.01	54.5	81.9
	100	0.0745	4.52	47.0	65.5
	210	0.0457	8.68	55.1	64.8
Zhang et al. [24]-avg	50	-0.130	2.53	45.2	56.1
	100	-0.0788	4.23	63.2	57.8
	210	-0.0772	8.97	96.3	63.4

For the maximum load capacity of the corroded bars, the $R_{pearson}$ values are all larger than 0.95, indicating that all three methods predict the trend of the load capacity with good accuracy, with the GMM method showing the least errors. For the prediction

of the deformation capacity, however, the three models show distinctive performances, with the GMM method exhibiting considerable improvement over the other two models. It should be noted that a main reason for the large errors in the predictions with the other two models lies in the fact that a fixed gauge was applied in the corresponding experiments. For example, Zhang et al. [23] measured the ultimate strain of reinforcement using a 50 mm gauge length. The corresponding model shows the smallest prediction error when it is applied to the same gauge length, but when the gauge length is increased from 50mm to 210mm, the *MAPE* value increases sharply from 43.9% to 113.1%.

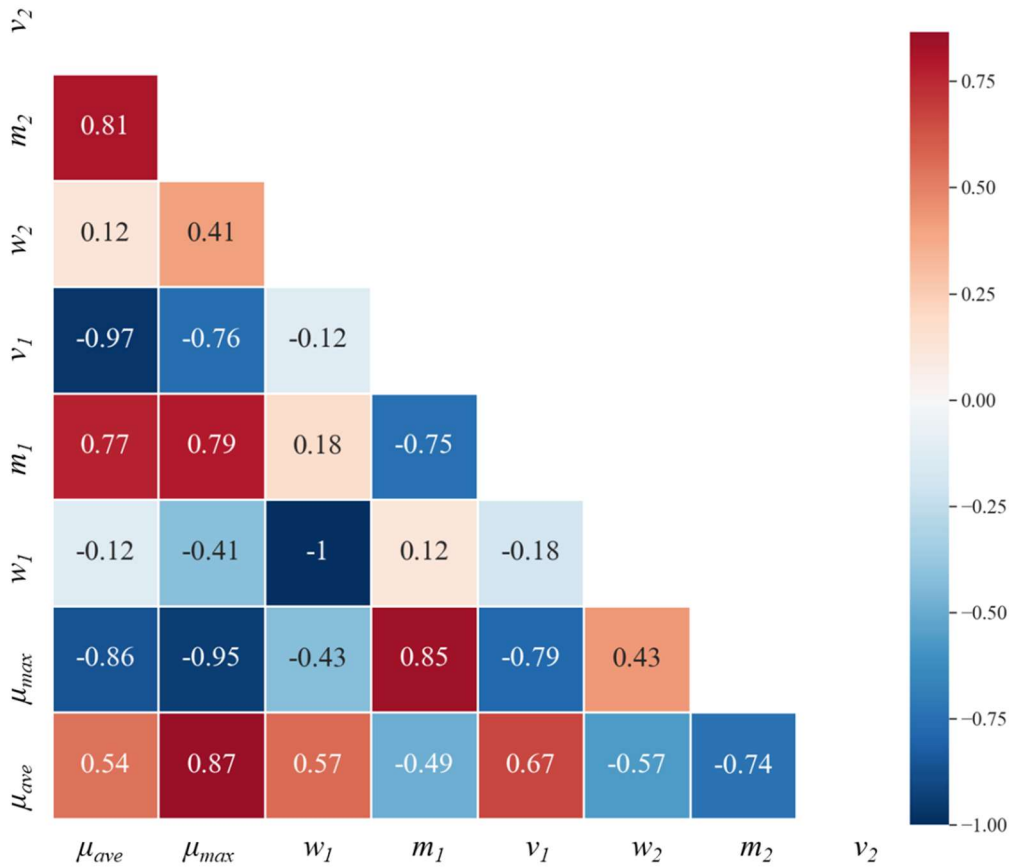**5 GMM-based method for time-varying mechanical properties of pitting bars**

Fig. 19. The correlation matrix of GMM parameters.

To facilitate the application of the probabilistic models presented in Section 3.4, a series of regression analyses on the GMM parameters are carried out and the time-varying results are presented in this section. The two-component GMM involves a total of six parameters, namely w_1, w_2, m_1, m_2, v_1 and v_2. To explore the correspondence among the GMM parameters and μ_{ave} as well as μ_{max}, the $R_{pearson}$ values of the above eight parameters are calculated one-to-one according to Eq. 19, and the correlation matrix is plotted in Fig. 19. The red squares represent positive correlations between the two parameters and the blue squares indicate negative correlations. The depth of the colour reflects the degree of correlation between the two parameters, with the specific $R_{pearson}$ values marked in the centre of the squares.

It is apparent that m_1 and v_1 show a stronger correlation with μ_{ave}, with $R_{pearson}$ values of -0.99 and 0.73, respectively. m_2 and v_2 exhibit a stronger correlation with μ_{max}, with $R_{pearson}$ values of -0.96 and 0.88, respectively. These results validate the hypothesis proposed in Section 3.4.

Based on the above observation, regression analyses are conducted for m_1 and v_1 with μ_{ave} as the independent variable, and for m_2 and v_2 with μ_{max} as the independent variable. The corresponding regression equations are given in Fig. 20 and Table 9.
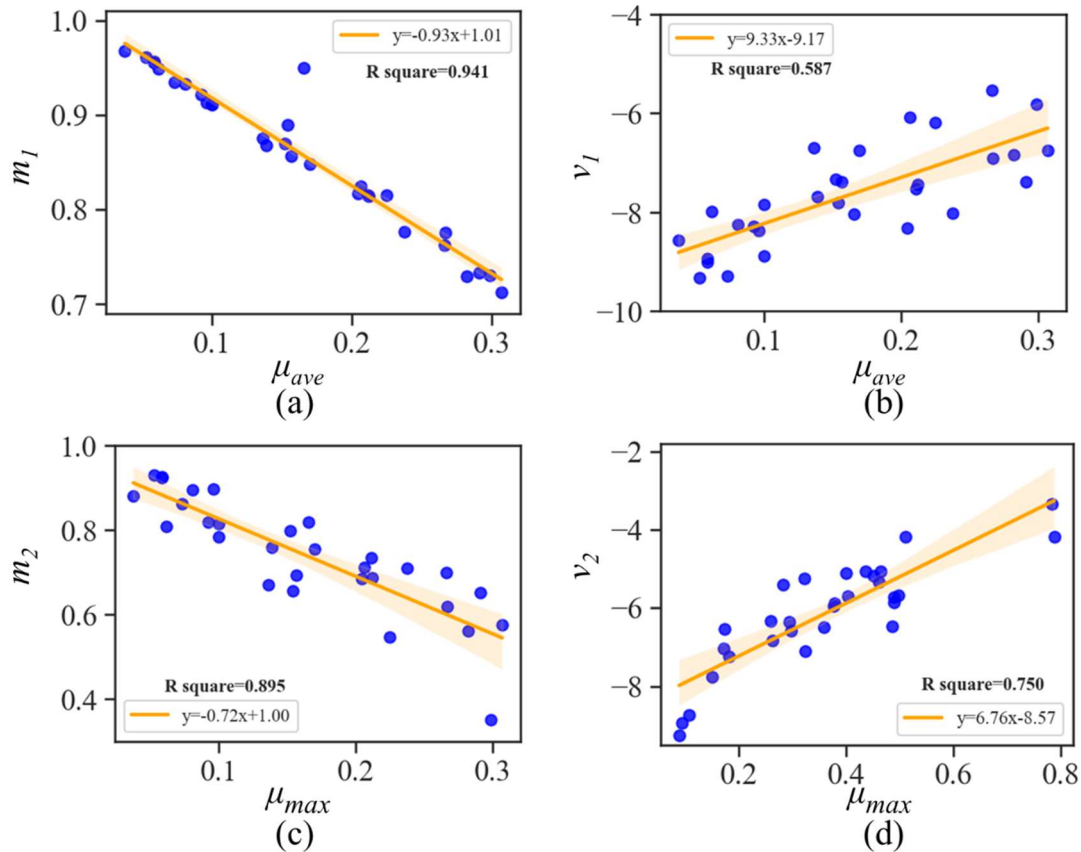

Fig. 20. The regression analysis of GMM parameters.

Table 9. The regression equations of GMM parameters.

Parameters/y	Arguments/x	Regression equation
μ_{max}	μ_{ave}	$y=1.69x+0.08$
m_1	μ_{ave}	$y=-0.93x+1.01$
v_1	μ_{ave}	$y=9.33x-9.17$
m_2	μ_{max}	$y=-0.72x+1.00$
v_2	μ_{max}	$y=6.76x-8.57$

The two weight coefficients, w_1 and w_2, are related to the proportion of pitting segments in the overall length and have no direct relation to the corrosion rate, with an absolute value of $R_{pearson}$ only 0.17 and 0.45. Due to $w_1+w_2=1$, they satisfy a strictly negative correlation with the $R_{pearson}$ value of -1. Therefore, the values of w_1 and w_2 can

be set flexibly according to engineering application or structural analysis requirements, as further discussed in Section 4.2.2. As a reference, the mean values of w_1 and w_2 for the 27 pitting bars prepared in this study are 0.7876 and 0.2124, respectively.

Based on the above analysis and results, it is feasible to estimate the degree of corrosion of the steel in RC structure under different service times and determine the degraded properties. A typical RC building located close to the coast and exposed to marine splash is taken as an example to comprehensively illustrate the utilization of the developed GMM and the realization of the whole calculation process. It is assumed that concrete cover x_c is 25 mm, the reinforcement diameter is 8 mm and the water cement ratio w/c is 0.5. The reinforcement corrosion in concrete consists of two main stages, namely the corrosion initiation stage and the corrosion propagation stage. Initial corrosion time is determined by the Duracrete model [51]:

$$T_0 = X_I \left\{ \frac{x_c^2}{4k_ek_tk_cD_0t_0^n} \left[\text{erf}^{-1} \left(\frac{C_s - C_{cr}}{C_s} \right) \right]^{-2} \right\}^{\frac{1}{1-n}} \tag{23}$$

Due to the various uncertainties involved in corrosion analysis, consider performing the Monte Carlo simulations with 50,000 samples to solve Eq. 23. The definition and the statistical distribution of each parameter in Eq. 23 can be found in [12, 52]. The mean value of results, 16.7 years, is taken as the time of corrosion initiation for the RC structure. Assume that the density of steel remains constant and the cross-sectional area of the bars decreases uniformly along the circumference. The average mass loss rate of the reinforcement can then be derived from Eqs. 24-26:

$$D_{cor}(t) = D_0 - 2e_{cor}(t) \tag{24}$$

$$e_{cor}(t) = 0.0116 \int_{T_0}^{t} i_{cor}(t)dt = \frac{0.5254(1 - w/c)^{-1.64}}{x_c}(t - T_0)^{0.71} \tag{25}$$

$$\mu_{ave}(t) = \frac{D_0^2 - D_{cor}^2(t)}{D_0^2} \tag{26}$$

where $D_{cor}(t)$ is the effective diameter of the bar at time t, D_0 is the original bar diameter, $e_{cor}(t)$ is the average corrosion depth of the bar at time t, and $i_{cor}(t)$ represents the corrosion current density at time t. Thereafter, following the regression equations provided in Table 9, a time-varying distribution model of the geometric properties of the corroded bars can be developed. Fig. 21 shows the time-varying GMMs for the distribution of reinforcement cross-sections during 50 years in service for the given building.
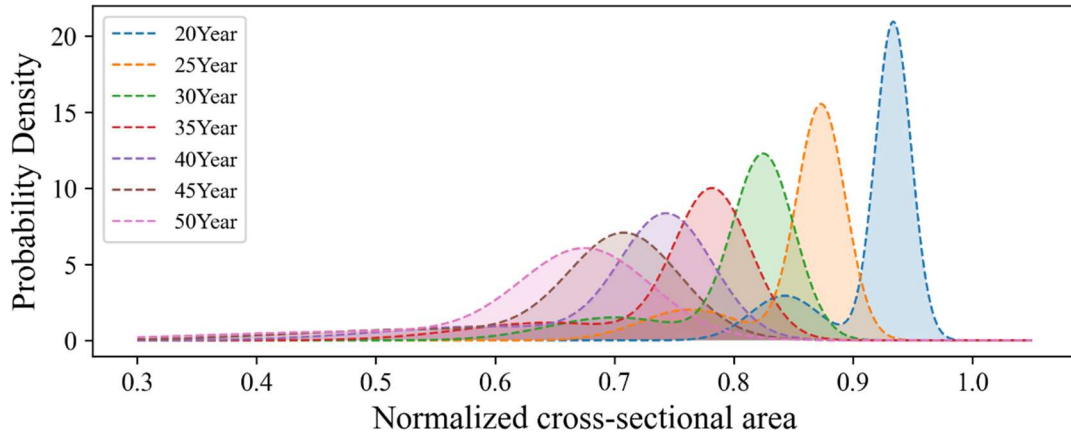
Fig. 21. The time-variant probabilistic density curves of GMM.

After the values of the GMM parameters are obtained, this calculation method allows for an adaptable determination of stress-strain relationships for reinforcement bars for any suitable (gauge) length an analyst or engineer chooses to use with respect to specific applications. Based on the calculation procedure in Section 4.2, a straightforward calculation flow chart is produced, as shown in Fig. 22. The calculation procedure is only for one point on the stress-strain curve of the corroded bar. In fact, the determined F_{max} can be divided equally into numerous nodes and then the procedure in Fig. 22 is repeatedly performed on these nodes to obtain the complete stress-strain curve for the corresponding corroded bar. Fig. 23 illustrates the deterioration of the tensile behaviour for the reinforcement in the service period.

It is worth noting that the GMM reflects a harsh corrosion scenario. Engineers can adjust the values of the coefficients in the GMM or even choose another probability model, such as the log-normal distribution model [27], depending on the possible corrosion pattern of the reinforcement. The analysis framework developed in this paper allows engineers to create more realistic uncertainty models for the reliability analysis of corroded RC structures and predict the cross-sectional loss as well as the residual mechanical properties of corroded reinforcement in a general way.
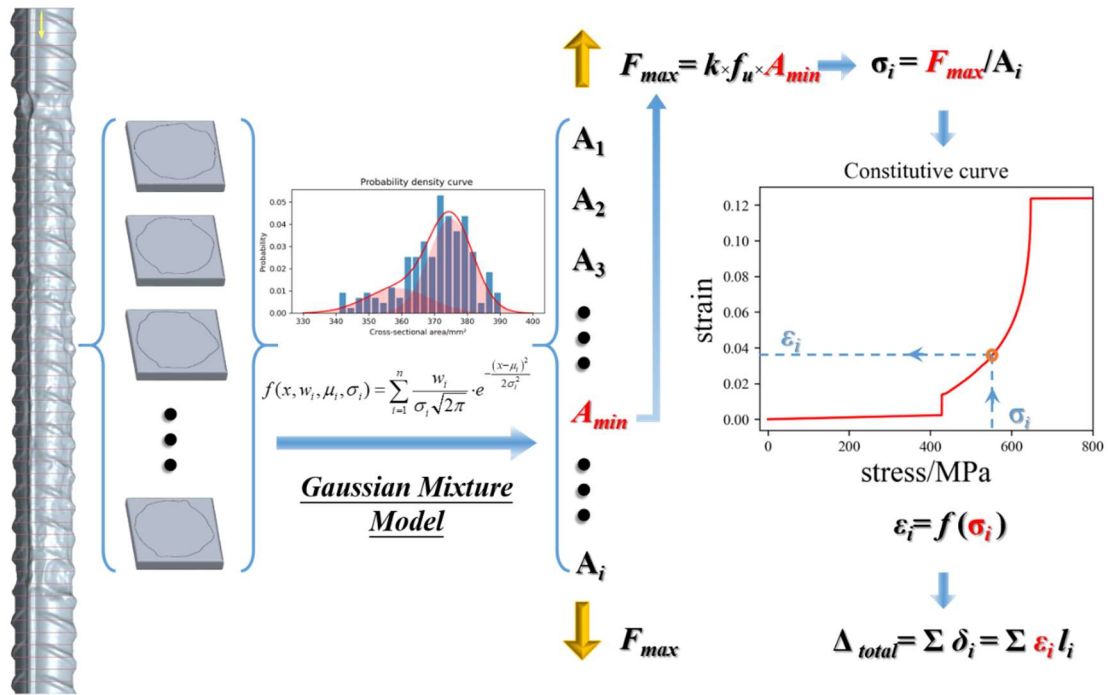
Fig. 22. Numerical scheme for evaluating the mechanical properties of corroded bars based on the corrosion morphology.
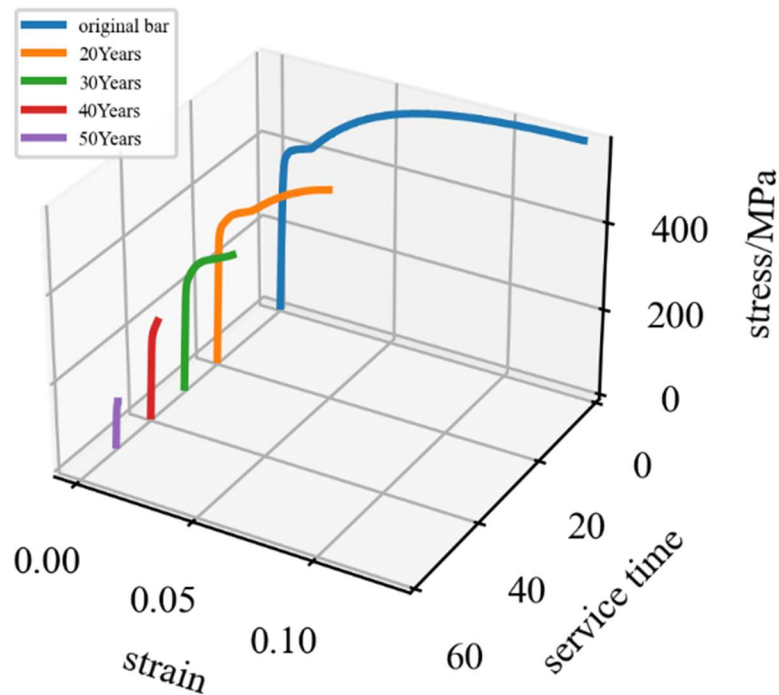

Fig. 23. Results of time-variant stress-strain curves.

6. Conclusions

In this paper, 27 non-uniform corrosion bars were prepared by the semi-immersion accelerated method. The corrosion morphology was precisely mapped using 3D scanning technology and then described with the Gaussian mixture model. The profile

35

analyses were conducted to evaluate the residual mechanical properties of corroded bars. The main conclusions can be summarized below:

(1) The semi-immersion accelerated corrosion method is suitable to produce corroded rebar specimens with a corrosion pattern similar to what occurs in real RC structures in a corrosive environment. The regression relationship between the maximum cross-sectional loss rate and the average cross-sectional loss rate, derived from these specimens, can be used to identify the non-uniform corrosion degree of steel bars under different corrosion conditions.

(2) Compared with classical unimodal distribution models, the two-component GMM can well characterise the residual cross-sectional distribution of pitting bars. The first Gaussian component with a higher weight (in a range of 0.6 to 0.9) represents the cross-sectional distribution of uniformly corroded segments, while the second Gaussian component with a lower weight (in a range of 0.1 to 0.4) represents the cross-sectional distribution of the pitting segments. The corresponding regression equations based on the corrosion level are provided.

(3) The tensile process of corroded bars can be well reproduced with a simplified theoretical method involving accumulating the deformations from all micro-segments based on the cross-sectional areas of the corroded rebar. The predicted values of the ultimate stress and strain from the theoretical analysis tends to be lower than the deformation values from the experiments, but the margin - generally within 20% - is considered as reasonable and this puts the predicted values on a reasonably conservative side for engineering applications.

(4) The degradation of the mechanical properties of corroded bars is mainly attributed to the loss of the effective cross-sectional area, while the intrinsic material properties remain unchanged. However, there exists a strengthening effect in the ultimate stress at the ultimate stage and this is not negligible. This enhancement effect is more significant as the diameter of the reinforcement increases.

(5) A GMM-based analytical method for evaluating the mechanical properties of pitting bars is proposed. Compared with the conventional method, this method incorporates the effects of the corrosion morphology, the original constitutive relationship and the bar diameter, thus enabling a more reliable prediction of the ultimate load capacity and the corresponding elongation for any sample (gauge) length of corroded bars.

The method proposed in this paper is of general applicability for the description of the mechanical properties of corroded steel bars. It should be noted that different corrosive environments and physical states of the RC components will affect the corrosion patterns of the steel bars, but these can be represented in specific parameters of the corrosion-related probability model. The subsequent research is to establish comprehensive probabilistic models with respect to the geometrical and mechanical properties of corroded bars for particular corrosive environments through a combination of actual structural data and laboratory simulation.

Declaration of Competing Interest

The authors declare that they have no known competing financial interests or personal relationships that could have appeared to influence the work reported in this paper.

Data availability

Data will be made available on request.

Acknowledgements

References

[1] L.W. Yu, R. Francois, V.H. Dang, V. L'Hostis, R. Gagne, Distribution of corrosion and pitting factor of steel in corroded RC beams, Constr Build Mater, 95 (2015) 384-392.

[2] Y.X. Zhao, X.Y. Xu, Y.Z. Wang, J.F. Dong, Characteristics of pitting corrosion in an existing reinforced concrete beam exposed to marine environment, Constr Build Mater, 234 (2020) 12.

[3] M.G. Stewart, Spatial variability of pitting corrosion and its influence on structural fragility and reliability of RC beams in flexure, Structural Safety, 26(4) (2004) 453-470.

[4] M.G. Stewart, Mechanical behaviour of pitting corrosion of flexural and shear reinforcement and its effect on structural reliability of corroding RC beams, Structural Safety, 31(1) (2009) 19-30.

[5] M.G. Stewart, Spatial and time-dependent reliability modelling of corrosion damage, safety and maintenance for reinforced concrete structures, Struct Infrastruct E, 8(6) (2012) 607-619.

[6] M. Zhang, N. Nishiya, M. Akiyama, S. Lim, K. Masuda, Effect of the correlation of steel corrosion in the transverse direction between tensile rebars on the structural performance of RC beams, Constr Build Mater 264 (2020).

[7] M. Zhang, H. Song, S. Lim, M. Akiyama, D.M. Frangopol, Reliability estimation of corroded RC structures based on spatial variability using experimental evidence, probabilistic analysis and finite element method, Eng Struct, 192 (2019) 30-52.

[8] J. Xin, M. Akiyama, S. Miyazato, D.M. Frangopol, S. Lim, Z. Xu, A. Li, Effects of galvanostatic and artificial chloride environment methods on the steel corrosion spatial variability and probabilistic flexural capacity of RC beams, Struct Infrastruct E, 18(10-11) (2022) 1506-1525.

[9] M. Zhang, M. Akiyama, M. Shintani, J. Xin, D.M. Frangopol, Probabilistic estimation of flexural loading capacity of existing RC structures based on

observational corrosion-induced crack width distribution using machine learning, Structural Safety, 91 (2021).

[10] S. Srivaranun, M. Akiyama, K. Masuda, D.M. Frangopol, O. Maruyama, Random field-based reliability updating framework for existing RC structures incorporating the effect of spatial steel corrosion distribution, Struct Infrastruct E, 18(7) (2021) 967-982.

[11] S. Lim, M. Akiyama, D.M. Frangopol, Assessment of the structural performance of corrosion-affected RC members based on experimental study and probabilistic modeling, Eng Struct, 127 (2016) 189-205.

[12] F. Pugliese, L. Di Sarno, Probabilistic structural performance of RC frames with corroded smooth bars subjected to near- and far-field ground motions, Journal of Building Engineering, 49 (2022).

[13] O. Özcan, H. Erdoğan, Seismic Performance Assessment of RC Buildings Reinforced with Plain Rebars, Journal of Performance of Constructed Facilities, 36 (2022).

[14] Z.W. Miao, Y.F. Liu, X.D. Geng, Y. Lu, Evaluation of seismic collapse resistance of reinforced concrete frames designed with nonlinear viscous dampers, Structures, 40 (2022) 960-976.

[15] E. Moreno, A. Cobo, G. Palomo, M.N. González, Mathematical models to predict the mechanical behavior of reinforcements depending on their degree of corrosion and the diameter of the rebars, Constr Build Mater, 61 (2014) 156-163.

[16] I. Fernandez, C.G. Berrocal, Mechanical Properties of 30 Year-Old Naturally Corroded Steel Reinforcing Bars, Int. J. Concr. Struct. Mater., 13 (2019) 19.

[17] Y.F. Liu, Z.W. Miao, C. Shen, X.D. Geng. Evaluation of mechanical properties of non-uniform corroded rebars based on Monte Carlo method, J. Jilin. Univ., (2023) (in Chinese).

[18] F. Tang, Z. Lin, G. Chen, W. Yi, Three-dimensional corrosion pit measurement and statistical mechanical degradation analysis of deformed steel bars subjected to accelerated corrosion, Constr Build Mater, 70 (2014) 104-117.

[19] X. Gu, H. Guo, B. Zhou, W. Zhang, C. Jiang, Corrosion non-uniformity of steel bars and reliability of corroded RC beams, Eng Struct, 167 (2018) 188-202.

[20] C.A. Apostolopoulos, S. Demis, V.G. Papadakis, Chloride-induced corrosion of steel reinforcement – Mechanical performance and pit depth analysis, Constr Build Mater, 38 (2013) 139-146.

[21] R. Rajagopal, S. Sharma, R.G. Pillai, S.J. Subramanian, Assessment of Stress-Strain Behavior of Corroded Steel Reinforcement Using Digital Image Correlation (DIC), J Test Eval, 46 (2018) 1874-1890.

[22] W.J. Zhu, R. Francois, C.S. Poon, J.G. Dai, Influences of corrosion degree and corrosion morphology on the ductility of steel reinforcement, Constr Build Mater,

148 (2017) 297-306.

[23] W.P. Zhang, D.F. Shang, X.L. Gu. Stress-Strain Relationship of Corroded Steel Bars, J. Tongji. Univ., 34 (2006) 586-592 (in Chinese).

[24] J.Z. Zhang, J. Huang, C.Q. Fu, L. Huang, H.L. Ye, Characterization of steel reinforcement corrosion in concrete using 3D laser scanning techniques, Constr Build Mater, 270 (2021) 16.

[25] S. Lim, M. Akiyama, D.M. Frangopol, H. Jiang, Experimental investigation of the spatial variability of the steel weight loss and corrosion cracking of reinforced concrete members: novel X-ray and digital image processing techniques, Struct Infrastruct E, 13(1) (2017) 118-134.

[26] G. Wang, Y. Ma, L. Wang, J. Zhang, Experimental study and residual fatigue life assessment of corroded high-tensile steel wires using 3D scanning technology, Engineering Failure Analysis, 124 (2021) 105335.

[27] M.M. Kashani, A.J. Crewe, N.A. Alexander, Use of a 3D optical measurement technique for stochastic corrosion pattern analysis of reinforcing bars subjected to accelerated corrosion, Corros Sci, 73 (2013) 208-221.

[28] M. Tahershamsi, I. Fernandez, K. Lundgren, K. Zandi, Investigating correlations between crack width, corrosion level and anchorage capacity, Struct Infrastruct E, 13 (2017) 1294-1307.

[29] X. Sun, H. Kong, H. Wang, Z. Zhang, Evaluation of corrosion characteristics and corrosion effects on the mechanical properties of reinforcing steel bars based on three-dimensional scanning, Corros Sci, 142 (2018) 284-294.

[30] J. Xia, W.-l. Jin, Y.-x. Zhao, L.-y. Li, Mechanical performance of corroded steel bars in concrete, Proceedings of the Institution of Civil Engineers - Structures and Buildings, 166(5) (2013) 235-246.

[31] U. Angst, B. Elsener, A. Jamali, B. Adey, Concrete cover cracking owing to reinforcement corrosion–theoretical considerations and practical experience, Materials and corrosion, 63 (2012) 1069-1077.

[32] C.G. Berrocal, I. Fernandez, R. Rempling, The interplay between corrosion and cracks in reinforced concrete beams with non-uniform reinforcement corrosion, Mater Struct, 55 (2022).

[33] J. Xia, J. Chen, T. Li, J. Shen, Q. Liu, W. Jin, Modelling the corrosion mechanism of steel bars in chloride-contaminated concrete with transverse cracks, Mag Concrete Res, (2023) 1-15.

[34] C.Q. Fu, N.G. Jin, H.L. Ye, X.Y. Jin, W. Dai, Corrosion characteristics of a 4-year naturally corroded reinforced concrete beam with load-induced transverse cracks, Corros Sci, 117 (2017) 11-23.

[35] Y. Peng, Z. Wang, F. Gong, Y. Zhao, T. Meng, W. Jin, K. Maekawa, Spatial characteristics of stray current corrosion of reinforcing bars in pseudo concrete,

Struct Concrete, (2022).

[36] E. Chen, C.G. Berrocal, I. Fernandez, I. Lofgren, K. Lundgren, Assessment of the mechanical behaviour of reinforcement bars with localised pitting corrosion by Digital Image Correlation, Eng Struct, 219 (2020) 17.

[37] Y. Ma, Y. He, G. Wang, L. Wang, J. Zhang, D. Lee, Corrosion fatigue crack growth prediction of bridge suspender wires using Bayesian gaussian process, Int J Fatigue, 168 (2023) 107377.

[38] X. Wang, X. Song, M. Zhang, X. Du, Experimental comparison of corrosion unevenness and expansive cracking between accelerated corrosion methods used in laboratory research, Constr Build Mater, 153 (2017) 36-43.

[39] K. Andisheh, A. Scott, A. Palermo, D. Clucas, Influence of chloride corrosion on the effective mechanical properties of steel reinforcement, Struct Infrastruct E, 15 (2019) 1036-1048.

[40] National Standard of the People's Republic of China, Corrosion of metals and alloys—Removal of corrosion products from corrosion test specimens, GB/T 16545-2015, Beijing, 2016.

[41] A. Meda, S. Mostosi, Z. Rinaldi, P. Riva, Experimental evaluation of the corrosion influence on the cyclic behaviour of RC columns, Eng Struct, 76 (2014) 112-123.

[42] W.P. Zhang, B.B. Zhou, X.L. Gu, H.C. Dai, Probability Distribution Model for Cross-Sectional Area of Corroded Reinforcing Steel Bars, Journal of Materials in Civil Engineering, 26 (2014) 822-832.

[43] B. Zhou, X. Sun, D. Zou, H. Wang, Evaluation of corrosion morphology on mechanical properties of reinforcing steel bars using numerical simulation and simplified analytical model, Journal of Building Engineering, 52 (2022).

[44] National Standard of the People's Republic of China, Metallic materials-Tensile testing-Part 1: Method of test at room temperature, GB/T 228.1-2014, Beijing, 2014.

[45] C.M. Bishop, N.M. Nasrabadi, Pattern recognition and machine learning, Springer, 2006.

[46] K.P. Burnham, D.R. Anderson, Multimodel inference: understanding AIC and BIC in model selection, Sociological methods & research, 33 (2004) 261-304.

[47] R. Francois, I. Khan, V.H. Dang, Impact of corrosion on mechanical properties of steel embedded in 27-year-old corroded reinforced concrete beams, Mater Struct, 46 (2013) 899-910.

[48] D. Li, C. Xiong, T. Huang, R. Wei, N. Han, F. Xing, A simplified constitutive model for corroded steel bars, Constr Build Mater, 186 (2018) 11-19.

[49] C. Zeng, J.-H. Zhu, C. Xiong, Y. Li, D. Li, J. Walraven, Analytical model for the prediction of the tensile behaviour of corroded steel bars, Constr Build Mater, 258 (2020).

[50] W.D. Callister, D.G. Rethwisch, Fundamentals of materials science and engineering, Wiley London2000.

[51] DuraCrete, Statistical quantification of the variables in the limit state functions, The European Union-Brite EuRam III-Contract BRPR-CT95-0132-Project BE95-1347/R9, (2000).

[52] F. Pugliese, R. De Risi, L.D. Sarno, Reliability assessment of existing RC bridges with spatially-variable pitting corrosion subjected to increasing traffic demand, Reliability Engineering & System Safety, 218 (2022).